

Advanced Mott-Schottky heterojunction of semi-conductive MoS₂ nanoparticles/metallic CoS₂ nanotubes as an efficient multifunctional catalyst for urea-water electrolysis

Thi Luu Luyen Doan ^a, Dinh Chuong Nguyen ^b, Kyoungin Kang ^c, Anusha Ponnusamy ^c, Henry I. Eya ^d, Nelson Y. Dzade ^{d,*}, Cheol Sang Kim ^{a,c,e,**}, Chan Hee Park ^{a,c,e,**}

^a Division of Mechanical Design Engineering, School of Engineering, Jeonbuk National University, Jeollabuk-do Jeonju 54896, Republic of Korea

^b Department of Nano Convergence Engineering, Jeonbuk National University, Jeollabuk-do Jeonju, Jeonbuk 54896, Republic of Korea

^c Department of Bionanotechnology and Bioconvergence Engineering, Graduate School, Jeonbuk National University, Jeollabuk-do Jeonju 54896, Republic of Korea

^d Department of Energy and Mineral Engineering, Pennsylvania State University, University Park, PA 16802, United States

^e Department of Bionanosystem Engineering, Graduate School, Jeonbuk National University, Jeollabuk-do Jeonju 54896, Republic of Korea

ARTICLE INFO

Keywords:

Mott-Schottky heterojunction
MoS₂ nanoparticles/CoS₂ nanotubes
Multifunctional catalyst
Overall water splitting
Urea electrolysis

ABSTRACT

Metallic CoS₂ has attracted considerable interest for the catalysis of electrochemical reactions; however, its catalytic activity is still lower than that of commercial novel metal-based catalysts. Semiconductive 2H-MoS₂ also holds a high capability for catalysis. In this work, a rationally designed Mott-Schottky heterojunction of ultrasmall MoS₂ nanoparticles/CoS₂ nanotube arrays is constructed via an effective synthetic protocol. Because of the difference in the Fermi level of the metallic CoS₂ and semiconducting MoS₂, strong Mott-Schottky interaction occurs at their heterointerface to gain equalization, resulting in the optimization of intermediates adsorption energies, thereby favoring the reaction kinetics of hydrogen evolution reaction (HER), oxygen evolution reaction (OER), and urea oxidation reaction (UOR). Consequently, the proposed catalyst yields high current densities at small HER and OER overpotentials or low UOR potentials, small Tafel slopes, and desirable stability, confirming its excellent electrocatalytic activities for these key half-reactions toward significantly boosting water and urea electrolysis.

1. Introduction

In recent years, the ever-increasing environmental issue and energy demand are motivating scientists to explore alternative energies with sustainability, environment-friendliness, and cost-effectiveness to replace fossil fuels [1–3]. Given its clean nature and high gravimetric energy density, hydrogen (H₂) has become an ideal candidate to meet the global demand for pollution-free energy [4,5]. Several methods of H₂ production have been reported, and show super efficiency. Among them, electrochemical water splitting offers green methods of high-quality H₂ production [6,7]. Two crucial half-reactions, namely the hydrogen evolution reaction (HER) and oxygen evolution reaction (OER), take place on the cathode and anode to split water into H₂ and oxygen (O₂), respectively. In general, overall water splitting requires

highly active and stable electrocatalysts for both HER and OER to reduce their inevitable overpotential and the free energy barriers of adsorbed H- or O-contained intermediates [8,9]. Alternatively, urea electrolysis, as an energy-saving method of H₂ production, has captured considerable attention [10,11]. Typically, urea electrolysis is established by two half-reactions, the cathode HER and the anodic urea oxidation reaction (UOR). Encouragingly, the UOR can theoretically occur at a very low oxidation potential of ~0.37 V, whereas the theoretical oxidation potential of water is 1.23 V [12,13], making urea electrolysis more efficient than water splitting in energy terms. However, to meet the growing demand H₂ industry in the near future, high-efficiency HER and UOR electrocatalysts are necessary for urea electrolysis for further improvement of its performance toward maximizing H₂ production efficiency. The problem is that the benchmark commercial catalysts of HER, OER,

* Corresponding author.

** Corresponding authors at: Division of Mechanical Design Engineering, School of Engineering, Jeonbuk National University, Jeollabuk-do Jeonju 54896, Republic of Korea

E-mail addresses: nxd5313@psu.edu (N.Y. Dzade), chskim@jbnu.ac.kr (C.S. Kim), biochan@jbnu.ac.kr (C.H. Park).

and UOR are mostly based on noble metals, such as Pt, RuO₂, and IrO₂ [14–16]; the high cost and scarcity of these noble metals extremely inhibit the real applications of water splitting and urea electrolysis. Therefore, there is a growing tendency to explore and design advanced multifunctional electrocatalysts for HER, OER, and UOR to replace noble metal-based catalysts.

Metallic cobalt sulfide (CoS₂) (bandgap ≈ 0 eV) has emerged as one of the most representative TMSS-based electrocatalysts, because of its excellent electronic conductivity, great chemical stability, and low cost [17–19]. Nanotube structure can amplify the exposure of electrocatalytic active sites, effectively promote secondary species distribution, and benefit mass transfer to boost the reaction kinetics [20]. Considering the merits mentioned above, a smart strategy is to construct CoS₂ in nanotube form to offer as many catalytic active centers as possible. Unfortunately, some issues have emerged for CoS₂, such as its rather lower HER activity than that of the commercial Pt/C catalyst [21], and unsatisfactory performance for OER and UOR [22,23]. To overcome the drawbacks, in addition to enriching accessible catalytic active sites and accelerating charge/mass transfer, improving the intrinsic activities of CoS₂ toward optimization of its capability in adsorption/desorption intermediates has been essential [24,25]. Coupling the CoS₂ with other materials, such as semiconductive MoS₂, to form a heterostructure has been evidenced as an effective strategy [26]. On the one hand, the conductive CoS₂ can serve as an effective electronic transport part to increase the electrical conductivity of the entire electrocatalysts. On the other hand, inspired by the semiconductor characteristics of MoS₂ and the metallic nature of CoS₂, a Mott-Schottky interaction can be formed over the heterostructure surface. At the individual Mott-Schottky contact points, the electrons can spontaneously flow across the heterointerface, leading to the regulation of local charge distribution, and thereby tuning the adsorption of intermediate species [25,27]. One of the best merits of Mott-Schottky heterojunction is that even the regulation of electronic structure occurs at the interface; there is no disturbance of the crystal lattice and intrinsic structure of the catalyst, thus enhancing the catalytic activity without a negative effect on the catalyst stability [27].

Herein, we report an advanced multifunctional electrocatalyst, integrated Mott-Schottky heterojunction of MoS₂ nanoparticles (NPs)/CoS₂ nanotubes (NTs) grown directly on three-dimensional carbon cloth (CC) (denoted as MoS₂ NPs/CoS₂ NTs). Although many MoS₂/CoS₂ heterojunction catalysts have been reported for water splitting [28,29], there are rare reports of Mott-Schottky heterojunction of metallic CoS₂ and semiconductive MoS₂ for all HER, OER, and UOR electrocatalysis. In our proposed material, the Mott-Schottky interaction between semiconductor MoS₂ and metallic CoS₂ can regular the electronic structure of both MoS₂ and CoS₂ at the heterointerface toward greatly improved water splitting and urea electrolysis performance. Furthermore, the as-prepared MoS₂ NPs/CoS₂ NTs possesses the excellent advantage of geometrical structure. In the heterostructured composite, the uniform and ultrasmall MoS₂ NPs disperse over the surface of CoS₂ NTs, and they can expose as many active sites as possible and large contact area. Also, the CoS₂ NTs can support MoS₂ active material owing to their metallic property that causes excellent electrical conductivity, and their anti-agglomeration nature, while their hollow structure will offer more advantages than that of the solid structure, such as exposing more active sites and larger surface area, lowering length of mass/charge transport, and speeding up the release of generated gases. As expected, the MoS₂ NPs/CoS₂ NTs catalyst delivered a current density of 10 mA cm⁻² with overpotentials of 99.3 and 242.2 mV under HER and OER conditions, respectively. For the UOR process, the MoS₂ NPs/CoS₂ NTs catalyst shows excellent catalytic activity with a low potential of 1.31 V at the current density of 10 mA cm⁻². Importantly, the water splitting and urea electrolysis devices assembled using MoS₂ NPs/CoS₂ NTs as both cathode and anode outperform most multifunctional electrocatalysts in the literature. Our complimentary first-principles density functional theory (DFT) calculations reveal that the synergistic effect between the CoS₂

and MoS₂ is beneficial to the intrinsic electrical conductivity and both Co and Mo active species in terms of the favorable and optimum adsorption of H- and O-containing intermediates.

2. Experimental section

2.1. Chemical reagents

The 2-Methylimidazole (C₄H₆N₂, 99%), hydrochloric acid (HCl, 37%), acetone (CH₃COCH₃, ≥ 99.5%), cobalt(II) nitrate hexahydrate (Co(NO₃)₂·6 H₂O, ≥ 98%), ethanol (CH₃CH₂OH, 95%), thioacetamide (TAA, CH₃CSNH₂, 98%), sodium molybdate dihydrate (Na₂MoO₄·2 H₂O, ≥ 99.5%), dibenzyl disulfide (C₁₄H₁₄S₂, 98%), polyvinylpyrrolidone (PVP), Nafion (5 wt%), potassium hydroxide (KOH, ≥ 85%), platinum on carbon (Pt/C, 20 wt%), ruthenium(IV) oxide (RuO₂, 99.9%), and urea (NH₂CONH₂, ≥ 99.5%) were purchased from Sigma-Aldrich.

2.2. Synthesis of MoS₂ NPs/CoS₂ NTs material

Initially, the fabrication of the Co-MOF nanowires (NWs) was achieved via a modified solution method. The CC substrate was pre-treated by high-intensity sonication in 3.0 M HCl, acetone, and de-ionized (DI) water for 5 h each, respectively. The reactant solution was fabricated by mixing 2-methylimidazole (0.4 M), Co(NO₃)₂·6 H₂O (0.025 M), and 80 mL DI water. The pre-treated CC substrate was dipped sequentially in the reactant solution for 4 h, followed by taking out and rinsing with DI water. The immersion in the same solution was then repeated for 4 h to ensure the complete growth of Co-MOF NWs over the substrate surface. It was demonstrated that the growth process of Co-MOF NWs in the reactant solutions of Co²⁺ and 2-methylimidazole could involve the two stages [30]. During the early stage, the 2-methylimidazole molecules were adsorbed on the surface of CC substrate. In the second stage, these adsorbed 2-methylimidazole linkers coordinated with Co²⁺ ion in the reactant solution to form MOF NWs.

The Co-MOF NWs precursor was converted into CoS₂ NTs via a simple solvothermal reaction. Firstly, TAA (0.36 g) was dissolved in ethanol, and stirred for 0.5 h to achieve a transparent solution. The obtained solution and Co-MOF NWs were transferred simultaneously to a 100 mL Teflon-lined autoclave, and then heated to 90 °C for 3 h. The product was cleaned with DI water and ethanol, and dried at 60 °C for 12 h. During the synthesis, TAA was initially decomposed into S²⁻ ions when the temperature reached 90 °C. Then, these released S²⁻ ions combined with Co²⁺ ions on the surface of Co-MOF NWs to form a thin layer of CoS₂. With the increase in reaction time, the inner part of Co-MOF was gradually etched, donating more Co²⁺ ions to the reactant solution. In second stage, these released Co²⁺ ions migrated to the shell layer and combined with S²⁻ in the solution, resulting in the gradual growth of CoS₂ shell layer. Finally, the Co-MOF template was fully etched and simultaneously, hollow-structured CoS₂ nanotubes were formed [31].

At the same time, the MoS₂ NPs was prepared by a hydrothermal method. Typically, Na₂MoO₄·2 H₂O (0.4 g) was dispersed in 30 mL DI water, and sonicated for 0.5 h. Then, 30 mL ethanol solution of C₁₄H₁₄S₂ (0.38 g) was dropped into the above solution and sonicated for 0.5 h. The resulting solution was subsequently transferred to a 100 mL Teflon-lined autoclave, and heated to 180 °C for 20 h. When the reaction was completed, the obtained suspension was separated into two parts, including the supernatant (MoS₂ NPs) and black solid, by centrifugation at 10,000 rpm for 1.5 h.

Finally, the CoS₂ NTs was decorated with MoS₂ NPs by dipping in the solution consisting of MoS₂ NPs and PVP (1 wt%) at 30 °C for 10 min. The MoS₂ NPs/CoS₂ NTs product was then rinsed with DI water, and dried at 60 °C, prior to annealing at 400 °C (heating rate of 2 °C min⁻¹) for 2 h under N₂ atmosphere (flow rate of 100 sccm).

2.3. Material characterization

The as-synthesized materials were characterized by field emission scanning electron microscopy (FE-SEM) (Carl Zeiss, AG-SUPRA 40), transmission electron microscopy (TEM) (JEM-ARM200F), X-ray diffraction (XRD) (D/Max 2500 V/PC) with Cu-K α radiation ($\lambda = 1.54 \text{ \AA}$), and X-ray photoelectron spectroscopy (XPS) (Thermo Fisher Scientific Inc., USA). The N₂ adsorption-desorption isotherm of the as-synthesized materials was recorded using an ASAP 2020 Plus system (Micromeritics Instrument Corp., USA).

2.4. Electrochemical characterization

All electrochemical measurements were carried out on CH Instruments CHI660D Electrochemical Workstation (USA). A typical three-electrode configuration, including the as-synthesized material as the working electrode, graphite rod as the counter electrode, and Ag/AgCl as the reference electrode, was assembled to evaluate the electrocatalytic performance for HER, OER, and UOR. Meanwhile, a two-electrode configuration, including the as-synthesized material as both the anode and cathode, was assembled to evaluate the overall water

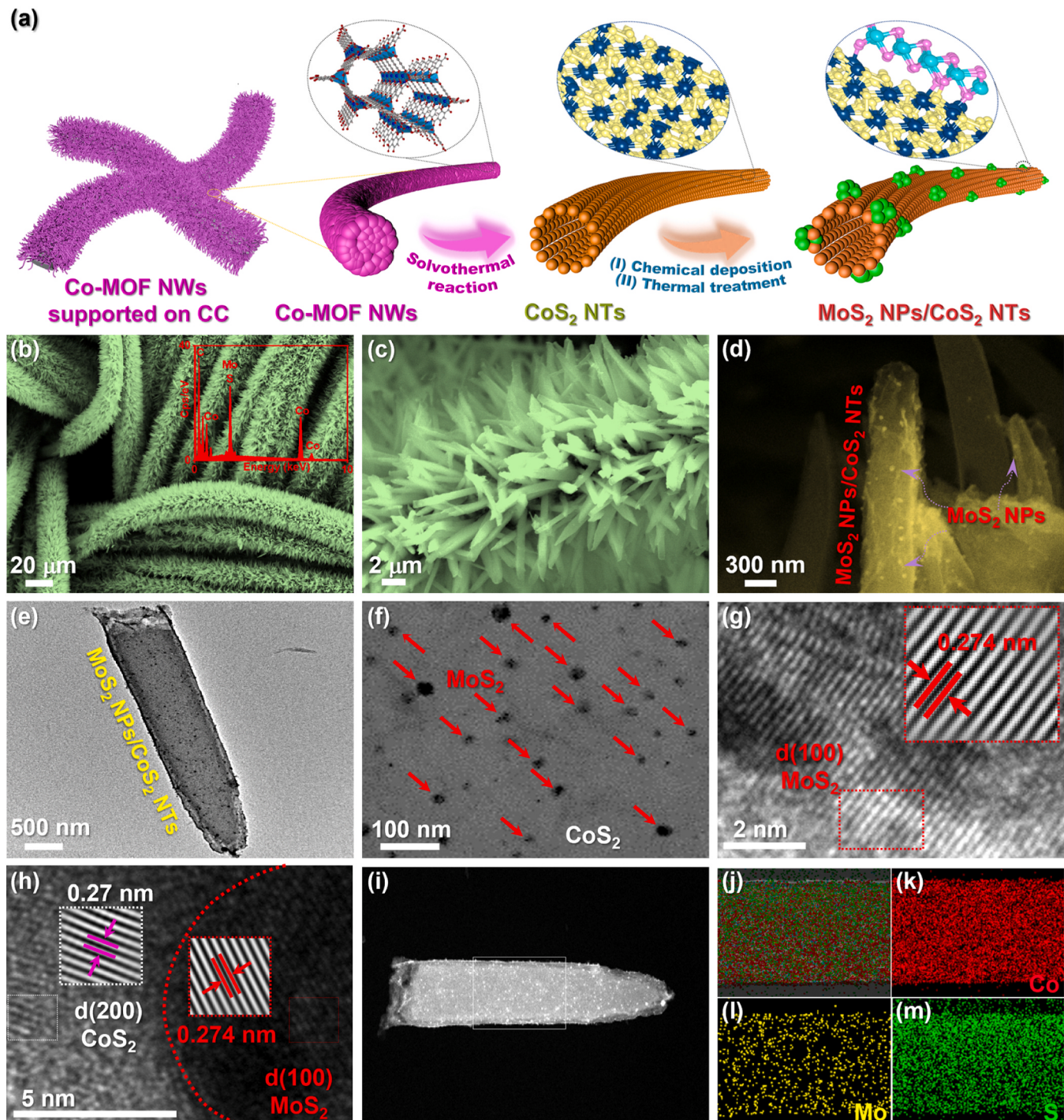


Fig. 1. (a) Schematic of the synthetic protocol of the MoS₂ NPs/CoS₂ NTs. (b)-(d) FE-SEM images of the MoS₂ NPs/CoS₂ NTs. Inset of (b): EDX spectral spectrum of the MoS₂ NPs/CoS₂ NTs. (e) and (f) TEM images of the individual MoS₂ NPs/CoS₂ nanotube. (g) and (h) HR-TEM images of the individual MoS₂ NPs/CoS₂ nanotube. (i) STEM image and (j)-(m) EDX mapping images of the individual MoS₂ NPs/CoS₂ nanotube.

splitting and urea electrolysis performances. The 1.0 M KOH solution was the electrolyte for the measurements of HER, OER, and water splitting, while 1.0 M KOH + 0.5 M urea or 1.0 M KOH + urine was the electrolyte for the measurements of UOR and urea electrolysis. Note that urine was collected from the same person in the morning. All potentials were reported on a reversible hydrogen electrode scale. Linear sweep voltammetry (LSV) curves were measured at a scan rate of 5 mV s^{-1} , and compensated for IR drop by the following equation:

$$E_{\text{IR-corr}} = E_{\text{mea}} - I \times R_s(V)$$

where, $E_{\text{IR-corr}}$, E_{mea} , I , and R_s are the IR-corrected potential (V), measured potential (V), measured current (A), and series resistance (Ω), respectively. The long-term stability test was executed using chronoamperometric measurement at a constant applied potential. Cyclic voltammetry (CV) curves were recorded at different scan rates to determine double-layer capacitance. Electrochemical impedance spectroscopy (EIS) was measured at the corresponding potential from 100 to 1000 Hz for the HER, OER, and UOR. Faradaic efficiency (FE) for HER and OER was determined by comparing the measured amount in the experiment and the theoretical amount of H_2 and O_2 , respectively.

3. Results and discussion

3.1. Morphological and structural characterization

The MoS₂ NPs/CoS₂ NTs were synthesized through a facile and effective approach. Fig. 1a illustrates the overall protocol to achieve the MoS₂ NPs/CoS₂ NTs, which protocol can be separated into four main stages. Initially, vertically aligned Co-based metal-organic framework (MOF) nanowires were grown on the surface of CC substrate (labeled as Co-MOF NWs) by a modified solution method [32]. The morphologies of the pristine CC and Co-MOF NWs were confirmed by FE-SEM. Fig. S1 shows that the CC has a smooth surface, in contrast to the rough morphology of the Co-MOF NWs sample (Fig. S2), which shows that the surface of CC substrate is uniformly coated with one-dimensional MOF nanowires having an average diameter of around $\sim 600 \text{ nm}$. Note that no fracture or peeling-off between Co-MOF nanowires and the CC substrate can be observed, indicating the strong adherence of the Co-MOF on the substrate. Such good contact between active material and framework is beneficial to the migration and transference of electrons, bringing high catalytic performance and good stability to the entire sample [33]. The magnified SEM image in Fig. S2c also displays that the individual MOF nanowire has a smooth surface. The corresponding energy dispersive X-ray (EDX) spectra (Figs. S1d and S2d) confirm the chemical composition of the pristine CC and Co-MOF NWs, respectively. Notably, the signal of N element observed from the EDX spectrum of Co-MOF NWs indicates that this sample is composed of N-containing organic ligands [32]. In the second stage, the Co-MOF NWs were transformed into CoS₂ NTs supported on the CC substrate (labeled as CoS₂ NTs) by the solvothermal reaction. Fig. S3 shows the morphology of the resultant CoS₂ NTs sample, which reveals the retained homogeneous distribution of CoS₂ NTs with an average diameter of around $\sim 600 \text{ nm}$ over the whole surface of the CC substrate. However, the magnified SEM image (Fig. S3c) shows that the nanowires become hollow, demonstrating the successful conversion of a solid structure into a hollow structure. Clearly, as compared to the solid nanowire, the nanotube structure offers more advantages, such as the higher density of exposed active sites, larger contact area between active material and electrolyte, lower length of mass/charge transport, and more effective facilitation of the emission of gaseous species [34], which can be anticipated to endowing the catalyst with significantly improved behaviors for HER, OER, and UOR. The EDX spectrum in Fig. S3d proves the existence of C, Co, and S elements in the CoS₂ NTs. At the same time, the MoS₂ NPs were prepared by a simple hydrothermal reaction, followed by dispersal over the CoS₂ NTs surface to form MoS₂ NPs/CoS₂ NTs heterostructure through chemical

deposition combined with a thermal treatment. Fig. 1b-d show that there is no difference in morphology between the pristine CoS₂ NTs and MoS₂ NPs/CoS₂ NTs, apart from the existence of a large number of NPs over the NTs surface. Thus, after decorating with MoS₂ NPs, the feature of nanotube arrays is thoroughly retained in the MoS₂ NPs/CoS₂ NTs sample, resulting in inheriting all the morphological merits of the CoS₂ NTs sample. The EDX spectrum in the Inset of Fig. 1b shows that in addition to the signals of C, Co, and S elements, the peak corresponding to Mo elements is detected, reconfirming the success in attaching MoS₂ to the CoS₂ NTs surface.

The MoS₂ NPs/CoS₂ NTs sample was further characterized by TEM. Fig. 1e and f show that the individual MoS₂ NPs/CoS₂ nanotube is a hollow structure with a diameter of around $\sim 600 \text{ nm}$, which is well consistent with the SEM observation. Interestingly, the TEM images clearly shows the uniform confinement of the MoS₂ NPs with an average diameter of around $\sim 30 \text{ nm}$ on the wall of the CoS₂ NTs. The small size of MoS₂ NPs will remarkably enlarge the electrochemically active surface area and allow the exposure of more available active sites, leading to more effective utilization of the MoS₂ component toward improving the catalytic performance for electrochemical reactions [35]. Further, high-resolution TEM (HR-TEM) analysis was carried out. The distinct lattice fringes are observed from the HR-TEM images in Fig. 1g and h, suggesting the high crystallinity of the MoS₂ NPs/CoS₂ NTs sample. The lattice fringes observed at only the nanoparticle region with an interplanar spacing of 0.274 nm are identical with the (100) lattice plane of MoS₂ (Fig. 1g), reconfirming that the spherical nanoparticles are MoS₂. Meanwhile, the other lattice fringes with an interplanar spacing of 0.27 nm are associated with the (200) lattice plane of CoS₂ (Fig. 1h), providing strong evidence for the formation of CoS₂ phases within the MoS₂ NPs/CoS₂ NTs heterostructure. The HR-TEM images also show a distinct heterointerface marked with red line between the MoS₂ and CoS₂ phases; such interface is a specific characteristic of the heterostructure, and can be anticipated to be beneficial for the adsorption and/or desorption of intermediate species [27,36]. The elementary composition of MoS₂ NPs/CoS₂ NTs was confirmed once again by scanning TEM (STEM) (Fig. 1i) and EDX-assisted elemental mapping analysis (Fig. 1j-m), which exhibit the presence of three elements such as Co, Mo, and S within the whole nanotube. Therefore, the TEM measurement provides solid evidence for the successful integration of MoS₂ NPs and CoS₂ NTs into one unique heterostructure, which allows the formation of intimate Mott-Schottky contacts of these components, leading to further improvement of the electrocatalytic performance.

We then confirmed the crystal structure of the developed materials by XRD analysis. All XRD patterns in Fig. 2a reveal the two obvious diffraction peaks located at $2\theta = 26.2$, and 43.9° which can be ascribed to carbon (PDF# 03-0401) [37]. The XRD pattern of Co-MOF NWs demonstrates that the Co-MOF nanowires possess layered phases with the elementary composition of $\text{Co}(\text{mim})_2 \cdot (\text{Hmim})_{1/2} \cdot (\text{H}_2\text{O})_{3/2} \cdot (\text{C}_{10}\text{H}_{16}\text{N}_5\text{O}_{3/2}\text{Co})$ [32,38,39]. After sulfidation combined with thermal treatment, the CoS₂ NTs give a completely different XRD pattern, compared to that of the Co-MOF NWs precursor. Apart from the diffraction peaks belonging to the carbon, the other diffraction peaks of CoS₂ NTs can be attributed to the (200), (210), (211), (220), and (311) lattice planes of the cubic phase of CoS₂ (PDF# 41-1471) [40], testifying to the thorough conversion of Co-MOF into the CoS₂ phase. In the XRD pattern of the MoS₂ NPs/CoS₂ NTs, in addition to the diffraction peaks of the carbon and CoS₂, the additive diffraction peaks at $2\theta = 14.3$, 33.5 , 34.3 , and 60.3° belong to the (002), (101), (103) and (110) lattice planes of the hexagonal MoS₂ phase (PDF# 09-0312) [41]. Thus, the MoS₂ and CoS₂ components are detected in the MoS₂ NPs/CoS₂ NTs sample via XRD characterization, as additional evidence for the successful fabrication of this unique heterostructure via our large-scale approach.

Thereafter, XPS was executed to analyze the surface composition and valence states of the CoS₂ NTs and MoS₂ NPs/CoS₂ NTs. The whole XPS spectra in Fig. 2b corroborate the presence of the elements of C, Co, and S in the CoS₂ NTs and MoS₂ NPs/CoS₂ NTs, in line with the results of

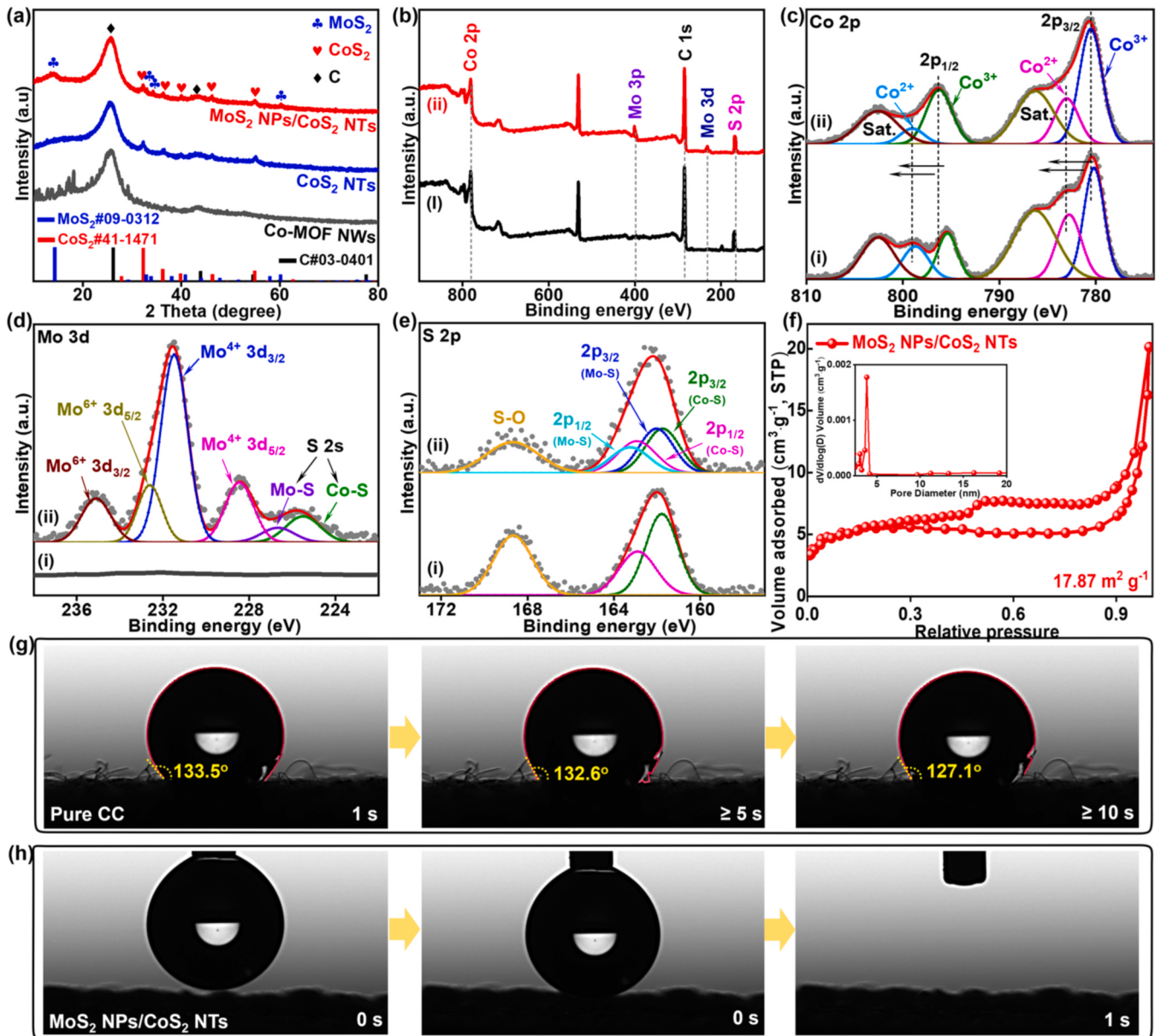


Fig. 2. (a) XRD patterns of the Co-MOF NWs, CoS₂ NTs, and MoS₂ NPs/CoS₂ NTs. (b) XPS survey spectra of (i) the CoS₂ NTs and (ii) the MoS₂ NPs/CoS₂ NTs. (c)-(e) High-resolution XPS spectra of the Co 2p, Mo 3d, and S 2p, respectively, for (i) the CoS₂ NTs and (ii) the MoS₂ NPs/CoS₂ NTs. (f) N₂ sorption isotherms of the MoS₂ NPs/CoS₂ NTs. Inset of (f): Pore distribution diagrams of the MoS₂ NPs/CoS₂ NTs. Contact angle measurements of (g) the pure CC, and (h) MoS₂ NPs/CoS₂ NTs.

EDX analysis. Furthermore, the Mo element in the XPS survey spectrum of MoS₂ NPs/CoS₂ NTs testifies to the confinement of MoS₂ NPs on the CoS₂ NTs. Fig. 2c presents the Co 2p XPS spectrum of the CoS₂ NTs and MoS₂ NPs/CoS₂ NTs, which are deconvoluted into two pronounced pairs of peaks, accompanied by their two shake-up satellite peaks (labelled as Sat.). The first pair of peaks located at binding energies of 780.1 and 795.3 eV belong to the 2p_{3/2} and 2p_{1/2} spin-states of Co³⁺, respectively, while the other pair of peaks at binding energies of 782.7 and 798.6 eV match well the 2p_{3/2} and 2p_{1/2} spin-states of Co²⁺, respectively [42]. The emergence of the typical core-level peaks suggests that Co³⁺ and Co²⁺ states can be assigned to the cubic phase of CoS₂. Importantly, the peaks of Co 2p_{3/2} and Co 2p_{1/2} in the Co 2p XPS spectrum of MoS₂ NPs/CoS₂ NTs show a blue shift, in comparison to the pristine CoS₂ NTs, indicating that strong Mott-Schottky contacts take place at the hetero-interface between the CoS₂ and MoS₂ [27]. To fully comprehend the property of electron transfer within this Mott-Schottky heterojunction, we calculated work function of CoS₂ and MoS₂ via ultraviolet

photoelectron spectroscopy (UPS) analysis (see Supporting Information for calculation details). Based on UPS spectra in Fig. S4, binding energy of secondary-cutoff-edge of CoS₂ and MoS₂ is found to be 17.67 and 17.39 eV, respectively. According to the equation S10, work function of CoS₂ and MoS₂ are calculated to be 3.53 and 3.81. Clearly, when the Mott-Schottky heterojunction is formed between CoS₂ and MoS₂, electrons partially migrate from the lower work function CoS₂ species to MoS₂ species, resulting in the perturbation of the electron density on both sides of CoS₂ and MoS₂. Such charge redistribution of CoS₂ and MoS₂ favors the adsorption/desorption of intermediates for remarkably boosting reaction kinetics of the HER, OER, and UOR [42,43]. Encouragingly, the Mott-Schottky contacts will be of great significance for the electrocatalytic activity of the entire MoS₂ NPs/CoS₂ NTs and thus make an important contribution to the enhanced performance of overall water splitting and urea electrolysis. Fig. 2d presents the high-resolution XPS Mo 3d spectrum of the MoS₂ NPs/CoS₂ NTs. Clearly, the overlapping peaks of Mo 3d and S 2s of sulfur are observed from the Mo 3d XPS

spectrum. We can deconvolute the high-resolution Mo 3d spectrum into six core-level peaks. The first pair of peaks at a binding energy of 225.6 and 226.5 eV of S 2 s component belongs to Co–S and Mo–S bonds, respectively, affirming once again the co-existence of MoS₂ and CoS₂ in this heterostructure [44]. The second pair of core-level peaks corresponding to the 2p_{5/2} and 2p_{3/2} spin-states of Mo⁴⁺ species is found at binding energies of 228.4 and 231.5 eV, respectively, belonging to the semiconducting MoS₂. Notably, a typical peak of the MoS₂ NPs/CoS₂ NTs has red shifted, in comparison to that of the pure MoS₂ NPs sample, as shown in Fig. S5, confirming the strong Mott-Schottky interaction between the CoS₂ and MoS₂. The final pair of core-level peaks at binding energies of 232.6 and 235.1 eV is consistent with the 3d_{5/2} and 3d_{3/2} spin-states, respectively, of the Mo⁶⁺ in MoO₃, which suggests the surface oxidation of the MoS₂ NPs/CoS₂ NTs sample in air [44]. With regard to the high-resolution XPS S 2p spectrum of CoS₂ NTs (Fig. 2e), the pair of S 2p_{3/2} and S 2p_{1/2} peaks centered at binding energies of 161.7 and 162.9 eV, respectively, should be attributed to Co–S bond in the CoS₂ phase [44,45]. In addition, the appearance of peaks at binding energies of 168.7 eV corresponding to S–O bond proves that the surface of sulfide species is partially oxidized [45]. For the S 2p spectrum of the MoS₂ NPs/CoS₂ NTs, in addition to the typical peaks belonging to the Co–S and S–O bonds, the other pair of peaks at 162.0 and 163.2 eV well indexes the S 2p_{3/2} and S 2p_{1/2}, respectively, from the Mo–S bond of MoS₂ [45], corroborating the existence of two phases of CoS₂ and MoS₂ in our developed material. Therefore, the results mentioned above further clarify that the MoS₂ NPs/CoS₂ NTs is successfully achieved by our proposed facile and effective approach. Meanwhile, the Mott-Schottky contacts are presented between the MoS₂ NPs and CoS₂ NTs at the heterointerfaces; such interfacial interaction can be anticipated to be advantageous for the electrocatalytic behavior of the entire MoS₂ NPs/CoS₂ NTs catalyst.

The structure of MoS₂ NPs/CoS₂ NTs was further characterized by N₂ adsorption-desorption measurement (Fig. 2f). The isothermal curve shows a large adsorption volume, suggesting a desirable specific surface area. Indeed, the MoS₂ NPs/CoS₂ NTs has a large specific surface area, of up to 17.87 m² g⁻¹, which is superior to that of other transition metal-based catalysts reported elsewhere, such as NiSe₂/CC with 10 m² g⁻¹ [46], CoP₃-HS with 15.1 m² g⁻¹ [47], and FeNi₂P with 6.25 m² g⁻¹ [48]. The Inset of Fig. 2f illustrates the corresponding pore size distribution of MoS₂ NPs/CoS₂ NTs, proving the presence of lots of mesopores ranging from 2 to 4 nm in its fine-heterostructure. Such large specific surface area and excellent mesoporous structure of MoS₂ NPs/CoS₂ NTs will expose more catalytic active sites and provide abundant holes to facilitate the electrolyte/active content movements, which are of great significance for the catalytic processes.

One of the most important properties of a porous structure is good permeability and high contact with the reactant/electrolyte, owing to its excellent porosity [49]. To evaluate these important properties of our MoS₂ NPs/CoS₂ NTs heterostructure, we conducted contact angle experiments. For comparison, the pristine CC substrate was also estimated by the contact angle test under the same conditions. As shown in Fig. 2g, the water contact angle of CC substrate is initially ~133.5°, after diffusion for 5 s is ~132.6°, and after more than 10 s is reduced to 127.1°, suggesting that the rate of water diffusion to the surface of CC substrate is rather slow. Whereas water diffusion to the surface of MoS₂ NPs/CoS₂ NTs electrode occurs immediately when dropping water on its surface, which is supported by the water contact angle of almost 0° from the beginning (Fig. 2l). Such rapid diffusion rate suggests the great wettability of the MoS₂ NPs/CoS₂ NTs electrode surface, which is conducive to the penetration of water-based electrolyte, ion transport, and shedding of generated gaseous species, thereby significantly speeding up the electrochemical efficiency of the catalytic electrode [48]. Consequently, it is precisely due to the vertically aligned nanotube heterostructure with huge specific surface area, excellent porosity, super hydrophilicity, and good Mott-Schottky contact between the components that the MoS₂ NPs/CoS₂ NTs can exhibit desirable electrocatalytic

behaviors.

3.2. Electrocatalytic performance

The electrocatalytic performances of the MoS₂ NPs/CoS₂ NTs and its derivatives, including the CoS₂ NTs, Co-MOF NWs, pristine CC substrate, and commercial Pt/C catalyst in HER, were estimated in a three-electrode configuration under alkaline condition (1.0 M KOH). Fig. 3a shows the IR-corrected LSV curves of different materials recorded at a scan rate of 5 mV s⁻¹. Obviously, the current densities of MoS₂ NPs/CoS₂ NTs are the highest among its three counterparts, and close to that of the commercial Pt/C. For clarity, Fig. S6 compares the current densities of the materials at an overpotential of 200 mV. As seen, the MoS₂ NPs/CoS₂ NTs achieves the highest current density of 80.0 mA cm⁻², followed by the order of the CoS₂ NTs > Co-MOF NWs > pure CC at 18.7 > 4.9 > 3.8 mA cm⁻², respectively. To further testify to the better catalytic performance of the MoS₂ NPs/CoS₂ NTs, we compared its overpotentials and the references at current densities of 10 and 50 mA cm⁻², and Fig. S7a shows the result. The MoS₂ NPs/CoS₂ NTs yields 10 and 50 mA cm⁻² at overpotentials of 99.3 and 185.8 mV, respectively, much lower than those of 165.6 and 264.1 mV for the CoS₂ NTs, 261.9 and 367.0 mV for the Co-MOF NWs, and 290.5 and 509.0 mV for the pure CC. While the overpotentials of MoS₂ NPs/CoS₂ NTs are merely higher than those of Pt/C (42.5 and 113.6 mV at current densities of 10 and 50 mA cm⁻², respectively), they are lower than those of the transition metal-based electrocatalysts reported elsewhere at the same current densities (Fig. S7b, and Table S1). In addition, the MoS₂ NPs/CoS₂ NTs is also superior to the transition metal-based electrocatalysts reported elsewhere both in terms of Tafel slope, as seen in Table S1, indicating that the MoS₂ NPs/CoS₂ NTs is one of the best HER electrocatalysts in the literature. To examine the reaction kinetics, the Tafel slope values of the developed materials and Pt/C catalyst were calculated from the LSV by using the Tafel equation (Fig. 3b). The Tafel slope values of these materials follow the order Pt/C < MoS₂ NPs/CoS₂ NTs < CoS₂ NTs < Co-MOF NWs < pure CC at 55.1 < 64.4 < 110.2 < 123.0 < 224.5 mV dec⁻¹, respectively. Accordingly, the Tafel slope value of the MoS₂ NPs/CoS₂ NTs is close to that of the commercial Pt/C, and much lower than those of its counterparts, rendering a faster HER kinetics under the action of the MoS₂ NPs/CoS₂ NTs. More importantly, because of the Tafel slope value falling in the range (40–120) mV dec⁻¹, the HER activity over the MoS₂ NPs/CoS₂ NTs heterostructure is governed by the Volmer-Heyrovsky mechanism ($H_2O + e^- \rightarrow H_{ads} + OH^-$ (Volmer), $H_{ads} + H_2O + e^- \rightarrow H_2 + OH^-$ (Heyrovsky)) [50]. Apart from the remarkable catalytic activity, long-term electrocatalytic durability and stability are also essential criteria to evaluate the performance of catalytic materials. Thus, we estimated the durability of the MoS₂ NPs/CoS₂ NTs by chronoamperometry test, as presented in Fig. 3c. Unsurprisingly, the current density of the MoS₂ NPs/CoS₂ NTs shows a negligible increase during the measurement time, which is supported by the relatively high retention of current density (~90.1%), demonstrating that its electrocatalytic activity can maintain long-term durability for over 50 h. The large amount of H₂ bubbles that escaped from the surface of MoS₂ NPs/CoS₂ NTs electrode during chronoamperometric measurement testifies to its superior electrocatalytic property (Inset of Fig. 3c). Moreover, the LSV curve achieved after stability testing is compared with the initial one to further investigate the stable properties of the MoS₂ NPs/CoS₂ NTs. Figs. S7c and d show that after 50 h testing, the overpotential positively shifts very little, as favorable evidence for the good stability of the MoS₂ NPs/CoS₂ NTs under the HER environment. The continuous CV scanning for 2000 cycles was performed for the MoS₂ NPs/CoS₂ NTs to further evaluate its stability. Fig. S8a shows that the LSV curve recorded after 2000 CV cycles almost overlaps with the initial one, suggesting that the catalytic performance of the MoS₂ NPs/CoS₂ NTs material is almost unchanged after continuously CV scanning. The HER overpotentials at current densities of 10 and 50 mA cm⁻² of the MoS₂ NPs/CoS₂ NTs after

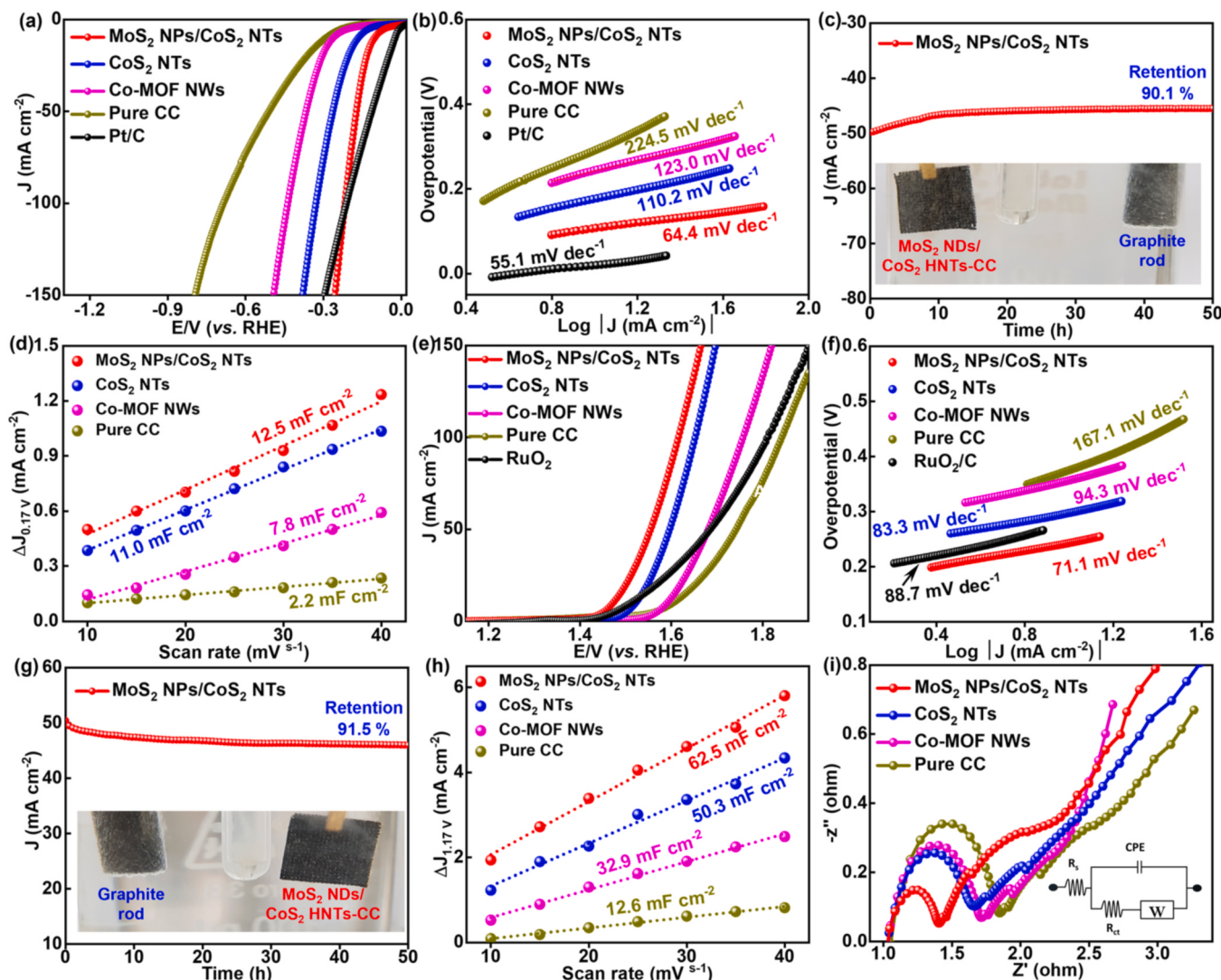


Fig. 3. HER activity of the as-synthesized materials in alkaline condition: (a) IR-corrected LSV curves and (b) corresponding Tafel plots of the pure CC, Co-MOF NWs, CoS₂ NTs, MoS₂ NPs/CoS₂ NTs, and Pt/C; (c) chronoamperometric curve of the MoS₂ NPs/CoS₂ NTs; (d) C_{dl} of the pure CC, Co-MOF NWs, CoS₂ NTs, and MoS₂ NPs/CoS₂ NTs derived from current density versus the scan rate. OER activity of the as-synthesized materials in alkaline condition: (e) IR-corrected LSV curves and (f) corresponding Tafel plots of the pure CC, Co-MOF NWs, CoS₂ NTs, MoS₂ NPs/CoS₂ NTs, and RuO₂; (g) chronoamperometric curve of the MoS₂ NPs/CoS₂ NTs; (h) C_{dl} of the pure CC, Co-MOF NWs, CoS₂ NTs, and MoS₂ NPs/CoS₂ NTs derived from the current density versus scan rate; (i) Nyquist plots of the pure CC, Co-MOF NWs, CoS₂ NTs, MoS₂ NPs/CoS₂ NTs, and RuO₂.

CV testing are found to be 105.2 and 183.5 mV, respectively, which are nearly close to the initial values (Fig. S8b). The findings confirm that the MoS₂ NPs/CoS₂ NTs material can serve as highly stable electrocatalyst for the HER. To examine the structural stability, we carried out SEM, mapping, XRD, and XPS analyses for the post-HER MoS₂ NPs/CoS₂ NTs. We found that the post-HER MoS₂ NPs/CoS₂ NTs preserves its vertically aligned nanotube architecture well (Fig. S9a). The chemical composition is also well conserved after long-term test, which is confirmed by the co-existence of Co, S, and Mo within the post-HER MoS₂ NPs/CoS₂ NTs structure (Figs. S9b-d), and the emergence of all signals belonging to CoS₂ and MoS₂ phases from the XRD pattern of the post-HER MoS₂ NPs/CoS₂ NTs (Fig. S9e). The XPS spectra of the post-HER MoS₂ NPs/CoS₂ NTs also exhibit insignificant variations, in comparison with that of the virgin one (Figs. S9f-i), proving no variation of the surface composition and valance states of the MoS₂ NPs/CoS₂ NTs after continuous catalysis. The experimental results provide favorable evidence for the high chemical and structural durability of the MoS₂ NPs/CoS₂ NTs under the harsh HER conditions, leading to an excellent preservation of its catalytic activity in long-term operation. Thereafter,

we conducted CV and EIS measurements to explore the reason for the high catalytic activity of the MoS₂ NPs/CoS₂ NTs toward the HER. From the CV curves in the non-Faradaic region (Fig. S10), the double layer capacitance (C_{dl}) values are determined for the MoS₂ NPs/CoS₂ NTs and its derivatives. Fig. 3d shows that the MoS₂ NPs/CoS₂ NTs gives a big C_{dl} value (12.5 mF cm⁻²), which is the highest value of the four as-synthesized materials. By comparison, the C_{dl} values of the CoS₂ NTs, Co-MOF NWs, and pure CC are only 11.0, 7.8, and 2.2 mF cm⁻², respectively. Such high C_{dl} value demonstrates that the MoS₂ NPs/CoS₂ NTs heterostructure possesses the largest electrochemically active surface area among the derivatives, and thus one fact is indisputable – its catalytic activity for the HER is better than those of the CoS₂ NTs, Co-MOF NWs, and pure CC. In addition, the EIS measurement renders deep insight into the reaction kinetics of the MoS₂ NPs/CoS₂ NTs so that its great catalytic activity can be further explained. Fig. S11 shows that compared to the CoS₂ NTs with charge transfer resistance (R_{ct}) value of 0.55 Ω, Co-MOF NWs with R_{ct} value of 0.58 Ω, and pure CC with R_{ct} value of 0.71 Ω, the MoS₂ NPs/CoS₂ NTs heterostructure has a considerably lower R_{ct} value (0.52 Ω), meaning its more rapid HER kinetics

than the others, which is consistent with the calculated Tafel slope value. There is a high opinion of the benefits of small R_{ct} in electrocatalytic process owing to the facile migration of electrons on the surface of the proposed heterostructure. The three-dimensional vertically aligned nanotube array architecture of MoS₂ NPs/CoS₂ NTs is considered a major reason for such excellent conductivity, associated with the ease of electrolyte infiltration and short path of ion transfer [51]. Additionally, the strong Mott-Schottky interaction between the MoS₂ and CoS₂ components can accelerate the charge transfer rate, which also contributes to good capability for charge transfer of the entire heterostructure.

The electrocatalytic OER performance is then estimated. Fig. 3e shows the IR-corrected LSV curves for MoS₂ NPs/CoS₂ NTs, together with its derivatives and benchmark RuO₂ catalyst for comparison. In particular, the MoS₂ NPs/CoS₂ NTs exhibits substantially improved electrocatalytic activity with lower overpotentials of 242.2 and 335.8 mV to achieve current densities of 10 and 50 mA cm⁻², respectively. Meanwhile, to drive the same current densities, the CoS₂ NTs, Co-MOF NWs, and pure CC samples require overpotentials of (293.4 and 363.5), (284.7 and 363.5), and (337.9 and 396.6) mV, respectively (Fig. S12a). The overpotentials of MoS₂ NPs/CoS₂ NTs are even considerably smaller than those of the benchmark RuO₂ catalysts with 335.4 and 438.9 mV at 10 and 50 mA cm⁻², respectively, and superior to those of the transition metal-based electrocatalysts for OER reported to date (Fig. S12b, and Table S2). Additionally, the Tafel slope of the MoS₂ NPs/CoS₂ NTs is also better than those of the transition metal-based electrocatalysts for OER reported to date (Table S2), confirming its better reaction kinetics for the OER. From the LSV results combined with the use of the Tafel equation, the Tafel slope values of all samples are determined to clarify the OER dynamics. Fig. 3f shows that a small Tafel slope of 71.1 mV dec⁻¹ is found for the MoS₂ NPs/CoS₂ NTs. This value is much smaller than those of the CoS₂ NTs, Co-MOF NWs, and pure CC of 83.3, 94.3, and 167.1 mV dec⁻¹, respectively, and even that of the commercial RuO₂ (88.7 mV dec⁻¹), manifesting that catalytic kinetics of MoS₂ NPs/CoS₂ NTs for the OER is the most robust among its counterparts and RuO₂. Such smallest overpotentials and Tafel slope values of MoS₂ NPs/CoS₂ NTs are solid evidence for its excellent OER activity. The chronoamperometric measurement was then conducted for the MoS₂ NPs/CoS₂ NTs under OER conditions to investigate its stable property, which is a significant criterion reflecting the catalyst's potential for practical applications. As displayed in Fig. 3g, the MoS₂ NPs/CoS₂ NTs shows a negligible decay in its current density by the continuous operation for 50 h, which is supported by the maintenance of more than 91.5% of the initial current density, demonstrating its exceptionally catalytic durability. During the stability testing, the abundant escape of O₂ gas is observed from the surface of MoS₂ NPs/CoS₂ NTs anode, confirming once again that the MoS₂ NPs/CoS₂ NTs can effectively catalyze the OER process (Inset of Fig. 3g). In addition, the LSV curve recorded after chronoamperometric testing almost coincides with the fresh one (Fig. S12c), while the overpotentials negligibly increase in comparison with the initial values (Fig. S12d). Likewise, after continuously CV scanning for 2000 cycles, the MoS₂ NPs/CoS₂ NTs shows negligible catalytic degradation, as seen in Fig. S13, further evidencing its excellent stability for the OER. The structural stability of the MoS₂ NPs/CoS₂ NTs under OER conditions is evaluated by SEM, mapping, XRD, and XPS analyses. The SEM image (Fig. S14a) indicates the unchanged morphology of the post-OER MoS₂ NPs/CoS₂ NTs compared to the fresh sample. The EDX mapping images (Figs. S14b-d) also reveal the presence of Co, S, and Mo elements. Additionally, no noticeable changes in the crystal phase are found for the post-OER MoS₂ NPs/CoS₂ NTs, as seen in its XRD pattern (Fig. S14e). Insight into the chemical composition and valance states of the post-OER MoS₂ NPs/CoS₂ NTs is achieved via XPS analysis (Figs. S14f-i). The high-resolution XPS Co 2p spectrum in the post-OER sample (Fig. S14g) reveals an increase in the intensity of Co³⁺ peaks, suggesting the formation of a higher oxidation state of Co species, such as CoOOH, associated with the partial oxidation of CoS₂

during the OER catalysis, which agrees well with the results in the literature [52,53]. Such in situ produced CoOOH species are conducive to the OER process, in that they are real OER active sites for speeding up the OER performance more effectively. Previous studies demonstrated by theoretical calculation that the formation of in-situ CoOOH species over the surface of the host materials during catalysis process of the OER not only optimized the Gibbs free energy changes of *OH, *O, and *OOH intermediate adsorption on the catalyst surface but also facilitated electron transfer, thus facilitating the OER process [54,55]. The Mo 3d spectrum (Fig. S14h) also reveals that the intensities of Mo⁶⁺ 3d_{5/2} and 3d_{3/2} are slightly higher than those of the fresh one, attributing to the possible oxidation of MoS₂ during the oxidation process. Also, the partial conversion of the sulfide phase (S²⁻) into sulfate phase (SO₄²⁻) and sulfite phase (SO₃²⁻) is observed from the S 2p spectrum of the post-OER MoS₂ NPs/CoS₂ NTs (Fig. S14i), supported by an increase in the intensity of the S–O peak; this further suggests the surface oxidation of the MoS₂ NPs/CoS₂ NTs during the OER catalysis. Therefore, the MoS₂ NPs/CoS₂ NTs possesses both excellent catalytic behavior and good stability for the OER. The Mott-Schottky heterojunction of the MoS₂ NPs/CoS₂ NTs still exists even after continuous catalysis of the OER for 50 h (Fig. S15), donating the almost intact catalytic property to the MoS₂ NPs/CoS₂ NTs.

In addition, the in situ surface oxidation during the OER catalysis also brings more real active sites to the heterostructure, thus further boosting its catalytic activity. To identify the origin of the promising OER catalytic performance of the MoS₂ NPs/CoS₂ NTs, on the one hand, the C_{dl} values are determined for the MoS₂ NPs/CoS₂ NTs and its derivatives. Through CV results recorded in the non-Faradaic region at various scan rates (Fig. S16), the C_{dl} value of 62.5 mF cm⁻² is determined for the MoS₂ NPs/CoS₂ NTs, which is among the highest values of the developed materials in this study, such as the CoS₂ NTs, Co-MOF NWs, and pure CC with 50.3, 32.9, and 12.6 mF cm⁻², respectively (Fig. 3h). The MoS₂ NPs/CoS₂ NTs has the highest C_{dl} value, reflecting its exposure of abundant catalytically active sites, and remarkably enhanced surface roughness, consistent with the excellent advantages of the heterostructure. On the other hand, EIS measurement was executed to further analyze the reaction kinetics of the OER. After simulating the Nyquist plots by an equivalent circuit (Fig. 3i), the R_{ct} values are found to be 0.37, 0.63, 0.67, and 0.79 Ω for the MoS₂ NPs/CoS₂ NTs, CoS₂ NTs, Co-MOF NWs, and pure CC, respectively. The MoS₂ NPs/CoS₂ NTs owns the lowest R_{ct} value among the as-synthesized materials and commercial RuO₂, indicating the best capability of charge transfer, which can boost the OER kinetics more effectively, in comparison with the others.

Despite the excellent HER and OER catalytic activities of MoS₂ NPs/CoS₂ NTs, which will bring superior overall water splitting efficiency, it is worth noting that high energy input of the water electrolyzer based on MoS₂ NPs/CoS₂ NTs is inevitable to produce H₂. Therefore, constructing an energy-saving device, such as a urea electrolyzer, is one of the most effective directions to achieve H₂ economy in the near future. Because in the urea electrolysis device, the HER is still the cathodic reaction, while the energy-saving UOR is an anodic reaction, instead of the conventional OER, we performed a series of suitable measurements for the MoS₂ NPs/CoS₂ NTs under UOR conditions to assess its UOR activity. Firstly, Fig. 4a presents the IR-corrected LSV curves of the MoS₂ NPs/CoS₂ NTs in the blank electrolyte (1.0 M KOH) and electrolyte with the addition of urea (1.0 M KOH + 0.5 M urea). The catalytic performance of the MoS₂ NPs/CoS₂ NTs in urea electrolyte is remarkably improved. In the introduction of urea, the MoS₂ NPs/CoS₂ NTs can achieve current densities of 10 and 50 mA cm⁻² at potentials of 1.31 and 1.44 V, respectively, which is 0.16 and 0.13 V lower than that in the blank electrolyte, respectively, suggesting that the MoS₂ NPs/CoS₂ NTs owns promising UOR catalytic behavior. For comparison, its derivatives, and the benchmark RuO₂ catalyst were also evaluated by LSV tests under urea conditions (Fig. 4b). As expected, the MoS₂ NPs/CoS₂ NTs needs the smallest potentials to achieve the same current densities, compared to the CoS₂ NTs, Co-MOF NWs, and pure CC. The catalytic performance of the MoS₂ NPs/CoS₂ NTs is even superior to that of the conventional

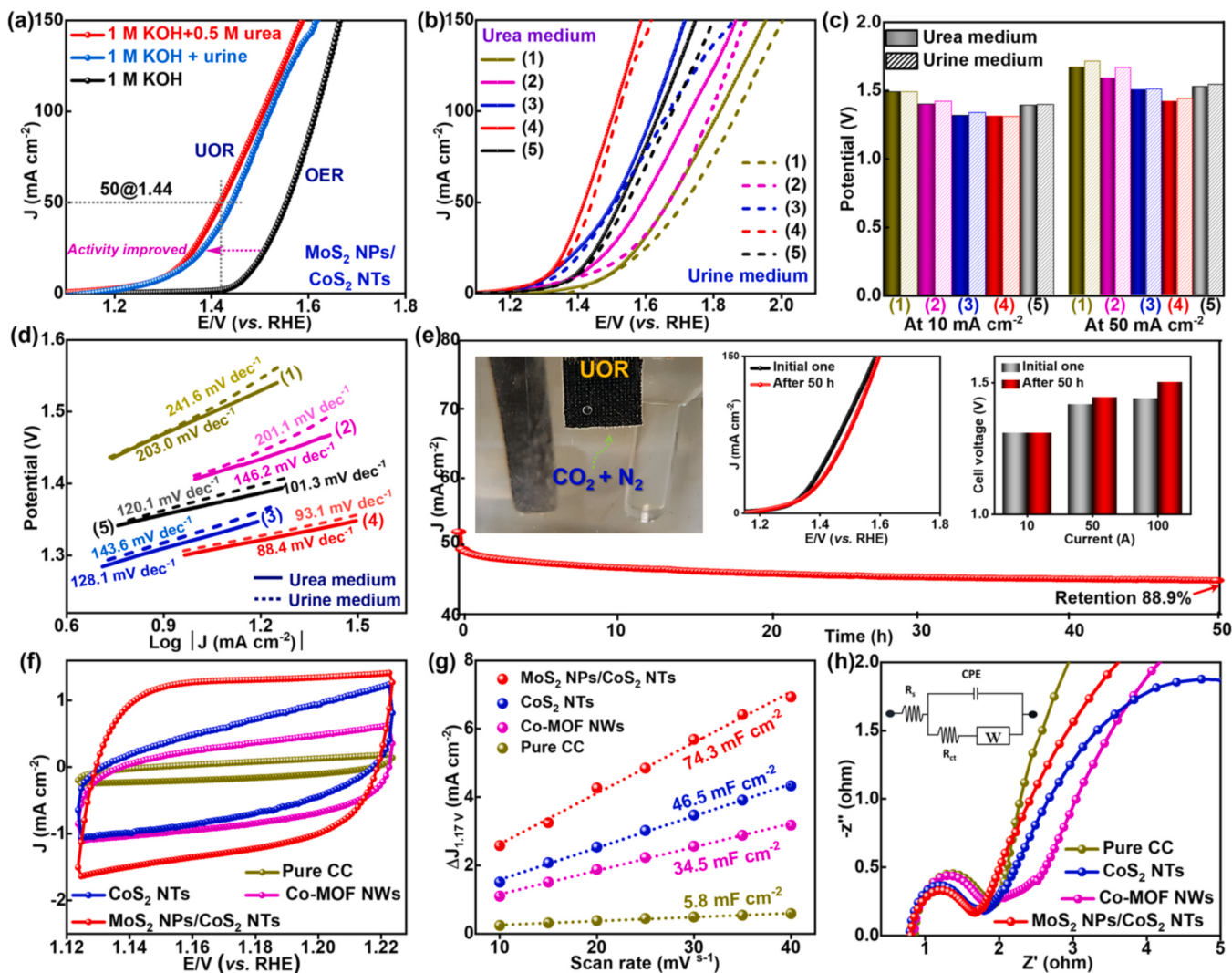


Fig. 4. UOR activity of the as-synthesized materials: (a) IR-corrected LSV curves of the MoS₂ NPs/CoS₂ NTs under OER (1.0 M KOH electrolyte) and UOR conditions (1.0 M KOH + 0.5 M urea as electrolyte or 1.0 M KOH + urine as electrolyte). (b) IR-corrected LSV curves, (c) corresponding potentials at 10 and 50 mA cm⁻², and (d) corresponding Tafel plots of (1) pure CC, (2) Co-MOF NWs, (3) CoS₂ NTs, (4) MoS₂ NPs/CoS₂ NTs, and (5) RuO₂ in the electrolyte with urea (1.0 M KOH + 0.5 M urea) or urine (1.0 M KOH + urine); (e) chronoamperometric curve of the MoS₂ NPs/CoS₂ NTs in the electrolyte with urea. Inset of the (e): LSV curves recorded before and after chronoamperometric testing and overpotentials at 10 and 50 mA cm⁻² determined before and after chronoamperometric testing; (f) CV curves of the pure CC, Co-MOF NWs, CoS₂ NTs, and MoS₂ NPs/CoS₂ NTs at a scan rate of 10 mV s⁻¹ in non-Faradaic region; (g) C_{dl} of the pure CC, Co-MOF NWs, CoS₂ NTs, and MoS₂ NPs/CoS₂ NTs derived from current density versus the scan rate; (h) Nyquist plots of the pure CC, Co-MOF NWs, CoS₂ NTs, MoS₂ NPs/CoS₂ NTs, and RuO₂.

RuO₂, making it competitive with commercial catalysts in industry applications. Fig. 4c shows that the potentials of MoS₂ NPs/CoS₂ NTs at 10 and 50 mA cm⁻² are considerably lower than those of the CoS₂ NTs, Co-MOF NWs, pure CC, and RuO₂ at (1.32 and 1.50), (1.40 and 1.59), (1.49 and 1.67), and (1.39 and 1.52) V, respectively. More interestingly, the MoS₂ NPs/CoS₂ NTs affords advanced UOR behavior surpassing almost all other electrocatalysts based on earth-abundant transition metals reported elsewhere both in terms of potential at 10 mA cm⁻² and Tafel slope, as illustrated in Fig. S17 and Table S3. Then, the UOR kinetics was studied by determining their Tafel slopes (Fig. 4d). Agreeing with the UOR performance, the MoS₂ NPs/CoS₂ NTs owns the smallest Tafel slope of 88.4 mV dec⁻¹, much smaller than those of the CoS₂ NTs, Co-MOF NWs, pure CC, and RuO₂ at 128.1, 146.2, 203.0, and 101.3 mV dec⁻¹, respectively. As such, it demonstrates that the reaction kinetics of UOR under the action of MoS₂ NPs/CoS₂ NTs is the most favorable. In other words, it suggests that building the Mott-Schottky heterojunction of CoS₂ and MoS₂ significantly accelerates mass/charge transfer and facilitates the intermediate adsorption/desorption, which is greatly conducive to the UOR performance. To further evaluate the potential of

MoS₂ NPs/CoS₂ NTs catalyst in practical applications toward the effective treatment of urea-rich wastewater, we have conducted LSV measurements for the MoS₂ NPs/CoS₂ NTs, its counterparts, and benchmark RuO₂ in electrolyte with urine (1.0 M KOH + urine), and Fig. 4a-d include the obtained results. Fig. 4a and b shows that the UOR performance of the products and RuO₂ in urine conditions is slightly lower than those in 0.5 M urea conditions. We also found that the UOR active trend in electrolyte with the addition of urine follows the order MoS₂ NPs/CoS₂ NTs > CoS₂ NTs > Co-MOF NWs > pure CC > RuO₂ (Fig. 4b and c), indicating the best catalytic activity of MoS₂ NPs/CoS₂ NTs in urine electrolyte. Furthermore, as shown in the Tafel plots (Figs. 4d), 93.1, 143.6, 201.1, 241.6, and 120.1 mV dec⁻¹ Tafel slope values are calculated for the MoS₂ NPs/CoS₂ NTs, CoS₂ NTs, Co-MOF NWs, pure CC, and RuO₂, respectively, in the urine electrolyte, demonstrating the best reaction kinetics of UOR under the help of the MoS₂ NPs/CoS₂ NTs. Such achieved results highlight the best catalytic performance of the MoS₂ NPs/CoS₂ NTs for the UOR in the urine electrolyte, thus confirming its great potential for practical applications in hydrogen production via urea electrolysis of the human urine. Furthermore, we also

conducted the electrochemical measurement for the products and RuO₂ in 0.33 M urea solution, as simulated human urine, for comparison, and the results are presented in Fig. S18. As we can see in Fig. S18a, there is a rather overlap between the LSV curve of the MoS₂ NPs/CoS₂ NTs sample in urine electrolyte and 0.33 M urea electrolyte, indicating that the electrochemical property of the MoS₂ NPs/CoS₂ NTs for the UOR in urine electrolyte is comparable to that in 0.33 M urea electrolyte. Likewise, Fig. S18b also displays that the electrocatalytic activity of the control samples, such as pure CC, Co-MOF NWs, and CoS₂ NTs, and the benchmark RuO₂ catalyst for the UOR in urine electrolyte is nearly close to those in the simulated human urine solution. However, the comparison in Fig. S18c exhibits that the potentials at current densities of 10 and 50 mA cm⁻² of these materials in urine electrolyte are slightly higher than those in 0.33 M urea electrolyte, suggesting the slightly lower catalytic performance for the UOR in the real urine solution. The Tafel slope values of the MoS₂ NPs/CoS₂ NTs, CoS₂ NTs, Co-MOF NWs, pure CC, and RuO₂ in urine electrolyte (Fig. S18d) are slightly higher than those in the simulated human urine as well, further suggesting that the kinetics of UOR in urine electrolyte is worse than that in 0.33 M urea electrolyte. This can be attributed to the effect of some interfering compounds, such as some organic salts and uric acid, on the UOR catalytic performance of the materials [13]. On the other hand, the findings in Fig. S18 also show that the electrocatalytic behavior of the MoS₂ NPs/CoS₂ NTs for the UOR is still the best among five samples even in the simulated human urine conditions, reconfirming the applicability of our proposed material in the urea electrolysis of real samples towards simultaneous treatment of urea-rich wastewater and production of green H₂ fuel. Concerning the effect of urea concentration on catalyst UOR performance, the LSV measurements performed for MoS₂ NPs/CoS₂ NTs in the alkaline electrolyte (1.0 M KOH) with the addition of different concentrations of urea (0.001, 0.002, 0.005, 0.01, 0.02, 0.05, 0.1, 0.5, and 1.0 M) and corresponding LSV curves are shown in Fig. S19a. As seen, with increasing urea concentrations up to 0.05 M, an obvious increase in the catalytic activity of MoS₂ NPs/CoS₂ NTs is observed, suggesting the superior sensitivity of our developed material for urea oxidation. Interestingly, the catalytic activity of MoS₂ NPs/CoS₂ NTs tends to be almost unchanged when the urea concentration exceeds 0.05 M, which must be assigned to the excess occupancy of active sites on the surface of the catalyst by the urea molecules and intermediate species at high urea concentrations [56]. The comparison of potentials at current densities of 10 and 50 mA cm⁻² (Fig. S19b) further confirms the phenomenon mentioned above. The stability of the MoS₂ NPs/CoS₂ NTs under urea conditions was studied by chronoamperometric testing. Fig. 4e displays that there is no identified change of current density after long-term working with a very high current retention of 88.9%, testifying that the MoS₂ NPs/CoS₂ NTs offers superior long-term stability. LSV measurement was further conducted for the post-UOR MoS₂ NPs/CoS₂ NTs. The negligible shift of LSV curve of the post-UOR MoS₂ NPs/CoS₂ NTs is discerned compared to the fresh one in the Inset of Fig. 4e. Further, slight enhancement of 27.2 and 61.6 mV potentials at 50 and 100 mA cm⁻² are found in the post-UOR MoS₂ NPs/CoS₂ NTs (Inset of Fig. 4e). Thus, even after 50 h of continuous working under UOR conditions, the catalytic activity of the MoS₂ NPs/CoS₂ NTs seems to be stable, which is one of the most pivotal items of evidence for the great potential of our developed catalyst in industrial application. The MoS₂ NPs/CoS₂ NTs was also tested by continuously CV scanning for 2000 cycles. As seen in Fig. S20, there is a negligible change in the catalytic performance of MoS₂ NPs/CoS₂ NTs after CV testing, corroborating its extraordinary stability for the UOR. The post-UOR MoS₂ NPs/CoS₂ NTs was investigated by SEM, EDX elemental mapping, XRD, and XPS analyses as well. Consistent with the obtained results of the virgin MoS₂ NPs/CoS₂ NTs, the SEM images, and SEM-EDX mapping images of the post-UOR MoS₂ NPs/CoS₂ NTs (Figs. S21a-d) prove the vertically aligned nanotube arrays architecture and the homogeneous distribution of Co, S, and Mo elements. Further, when compared with the XRD pattern of the virgin material (Fig. S21e), the XRD pattern of the

post-UOR MoS₂ NPs/CoS₂ NTs shows no significant change, manifesting that after long-term stability testing, its crystal phase is unchanged. The data of chemical composition and valence state of the post-UOR MoS₂ NPs/CoS₂ NTs are obtained by XPS analysis. Figs. S21f-i show the XPS spectra of the post-UOR MoS₂ NPs/CoS₂ NTs; the increase in intensities of Co³⁺ and Mo⁶⁺ peaks is observed from the high-resolution Co 2p and Mo 3d, respectively, and the partial conversion of metal–sulfur bonds to S–O bond is also discerned in the S 2p spectrum, testifying to the partial oxidation of the MoS₂ NPs/CoS₂ NTs surface during the UOR catalysis. This endows the catalyst with oxidation species that serve as additive electrocatalytic active sites, being considerably advantageous for the catalytic performance of the UOR process [57]. The intrinsic catalytic activity of the MoS₂ NPs/CoS₂ NTs for the UOR is partially clarified through calculating its C_{dl} values by CV measurements. Fig. S22 shows the CV curves at different scan rates of the MoS₂ NPs/CoS₂ NTs and its derivatives, such as the CoS₂ NTs, Co-MOF NWs, and pure CC. Fig. 4f displays that the MoS₂ NPs/CoS₂ NTs owns the highest current densities at the same scan rate of 10 mV s⁻¹. Consistent with this observation, the C_{dl} value of the MoS₂ NPs/CoS₂ NTs of 74.3 mF cm⁻² is the highest among the four materials, in which the C_{dl} values of the CoS₂ NTs, Co-MOF NWs, and pure CC are 46.5, 34.5, and 5.8 mF cm⁻², respectively (Fig. 4g). The unique nanotube nature of CoS₂ and the ultrasmall nanoparticle nature of MoS₂ can provide more accessible catalytic active sites, bringing the high C_{dl} value to the MoS₂ NPs/CoS₂ NTs. Such desirable C_{dl} can render the large electrochemically active surface area within the MoS₂ NPs/CoS₂ NTs, which can be recognized as a contributor to the significantly improved UOR activity. The R_{ct} values of the MoS₂ NPs/CoS₂ NTs and its counterparts were determined through EIS analyses as well (Fig. 4h). Remarkably, through simulating the EIS plots by an equivalent circuit (Inset of Fig. 4h), the R_{ct} value of the MoS₂ NPs/CoS₂ NTs is found to be 0.86 Ω, which is lower than those of the CoS₂ NTs (1.01 Ω), Co-MOF NWs (0.99 Ω), and pure CC (1.23 Ω), respectively, rendering the most outstanding capability of the MoS₂ NPs/CoS₂ NTs in charge transfer among those of the others. It must be concluded that the formation of the Mott-Schottky heterojunction can bring great improvement to the charge transfer process, and thus result in great improvement of the final UOR behavior of the MoS₂ NPs/CoS₂ NTs material. To further evaluate the potential of the MoS₂ NPs/CoS₂ NTs for industrial applications, we investigated its UOR activity under industrial-grade current densities. Initially, the catalytic performance of the MoS₂ NPs/CoS₂ NTs for OER and UOR at industrial-grade current densities was examined by LSV measurement. Corresponding IR-corrected LSV curves in Fig. S23a shows that the UOR performance of the MoS₂ NPs/CoS₂ NTs catalyst is still better than its OER performance even at high current density of 1000 mA cm⁻² or higher. We found that the UOR potentials of the MoS₂ NPs/CoS₂ NTs at current densities of 1000, 1100, and 1200 mA cm⁻² are 2.26, 2.34, and 2.41 V, respectively, much smaller than those under the OER conditions (0.209, 0.195, and 0.213 V) at the same current densities, demonstrating a great potential of our proposed material to substitute for the sluggish OER process in industrial applications. Next, we also performed LSV measurement to investigate the UOR activity of the as-synthesized catalysts under industrial-grade current densities, along with benchmark RuO₂ catalyst for comparison. As seen in Figs. S23b and c, at current density of 1000 mA cm⁻² or higher, the UOR potentials of the MoS₂ NPs/CoS₂ NTs are lower than those of its counterparts and RuO₂, providing the best UOR performance of the MoS₂ NPs/CoS₂ NTs at industrial-grade current densities. Concretely, when current density reached 1000, 1100, and 1200 mA cm⁻², the UOR potentials of the CoS₂ NTs are found to be 2.49, 2.53, and 2.59 V, respectively, Co-MOF NWs are 2.81, 2.89, and 2.97 V, respectively, pure CC are 3.31, 3.47, and 3.61 V, respectively, and RuO₂ are 2.56, 2.64, and 2.78 V, respectively, which are much higher than those of the MoS₂ NPs/CoS₂ NTs. To probe the long-term durability of the MoS₂ NPs/CoS₂ NTs under high current density conditions, chronoamperometric measurement was performed at a very high applied voltage of 2.26 V vs. RHE. The result in Fig. S23d shows that the MoS₂

NPs/CoS₂ NTs still maintains its excellent UOR activity even after continuously working at high potential for 40 h, supported by the relatively high current density retention of 74.6%. Therefore, it shows that the high catalytic performance of the proposed MoS₂ NPs/CoS₂ NTs for UOR under industrial-grade current densities can meet the requirements of real applications.

To exploit the benefits of the bifunctional MoS₂ NPs/CoS₂ NTs catalyst for the HER and OER processes (Fig. 5a), we applied the catalyst as both cathode and anode for overall water splitting in a lab-made water electrolyzer device (Fig. S24a). The LSV curves for overall water splitting in Fig. 5b display the high performance of the electrolyzer assembled using MoS₂ NPs/CoS₂ NTs, which performance is comparable to that of the one based on noble metals Pt/C (-) // RuO₂ (+). Indeed, the electrolyzer with MoS₂ NPs/CoS₂ NTs electrodes requires small cell voltages of 1.65 and 1.85 V to attain the current densities of 10 and 50 mA cm⁻², respectively. These cell voltage values are close to those of the electrolyzer using Pt/C (-) // RuO₂ (+) with 1.61 and 1.86 V at the same current densities (Fig. S25a). Furthermore, Fig. S25b, and Table S4 show that our developed material, MoS₂ NPs/CoS₂ NTs, reveals electrocatalytic performance for overall water splitting that greatly surpasses that of the non-noble metal electrocatalysts in the literature.

Additionally, by comparing the amount of gas generated in the experiment, which was measured by drainage method (Fig. S24b), with the amount of gas calculated in the theory, we determined the FE for the HER and OER processes during catalysis of overall water splitting (Fig. 5c). More surprisingly, the generated gas amount in the experiment is close to the calculated gas amount in the theory, and the molar ratio between H₂ and O₂ is found to be around 2: 1. In addition, the high FE values of 98.6% and 94.6% are found for the MoS₂ NPs/CoS₂ NTs during the HER and OER, respectively. Such FE values close to 100% of the MoS₂ NPs/CoS₂ NTs suggest that the MoS₂ NPs/CoS₂ NTs derives high current densities for overall water splitting from the evolution processes of H₂ and O₂ gases [36]. The long-term stability of the MoS₂ NPs/CoS₂ NTs was evaluated under overall water splitting environments by chronoamperometric testing. The electrolyzer based on the MoS₂ NPs/CoS₂ NTs shows marvelous stability with slight performance decay after long-term electrolysis for 50 h, supported by the high retention of the current density of up to 89.7% (Fig. 5d). In contrast, the electrolyzer with noble metal Pt/C (-) // RuO₂ (+) electrodes exhibits insufficient durability for overall water splitting, with remarkable degradation of its performance after only 30 h stability testing (Fig. 5d). Furthermore, the almost overlaps between the LSV curves recorded before and after

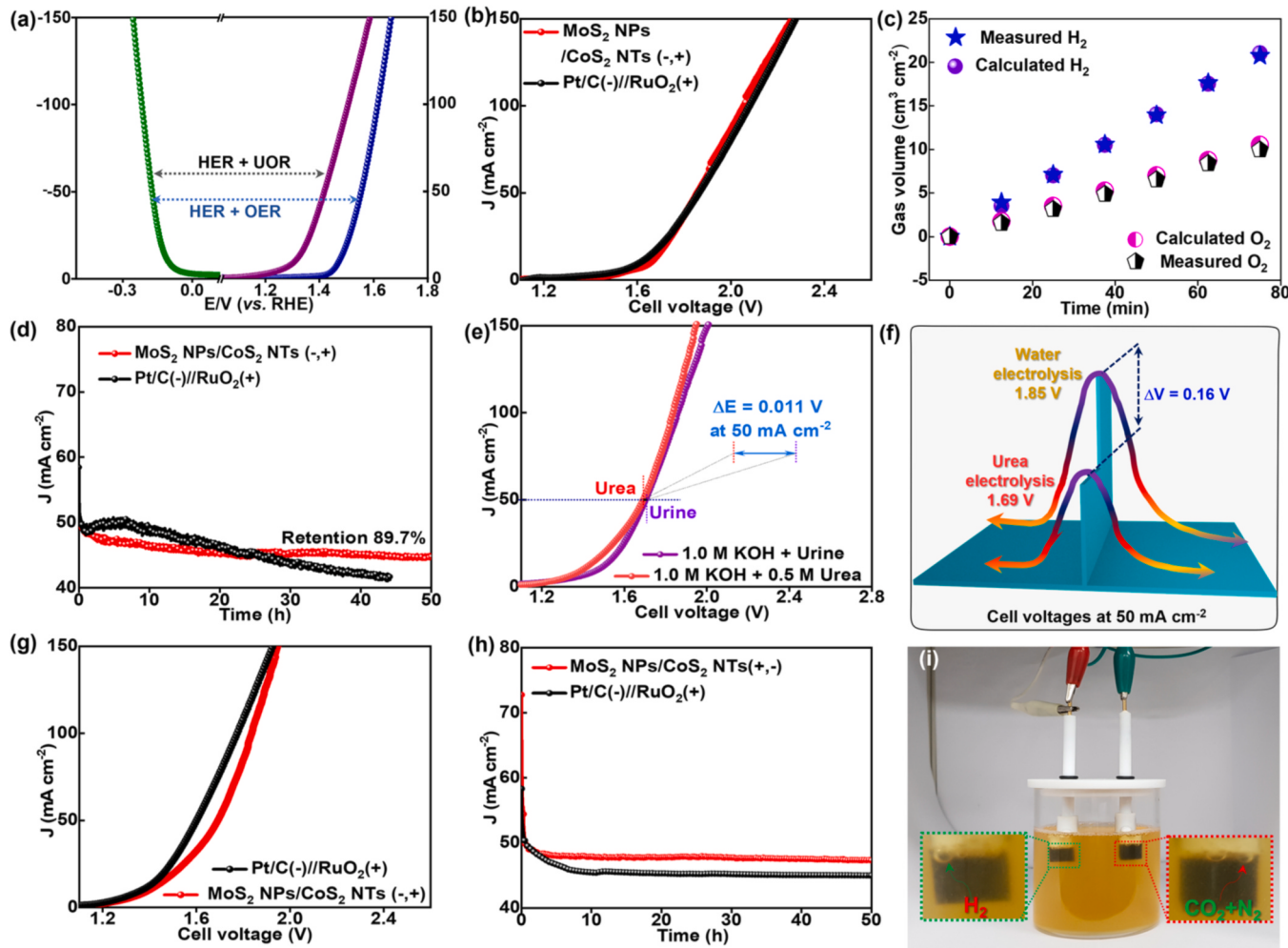


Fig. 5. (a) IR-corrected LSV curves of the MoS₂ NPs/CoS₂ NTs under HER, OER, and UOR conditions. Overall water splitting performance of the MoS₂ NPs/CoS₂ NTs in alkaline condition: (b) LSV curves of the MoS₂ NPs/CoS₂ NTs (-,+) and Pt/C (-) // RuO₂ (+); (c) amount of measured gas and calculated gas for MoS₂ NPs/CoS₂ NTs (-, +); (d) chronoamperometric curve of the MoS₂ NPs/CoS₂ NTs (-, +) under overall water splitting conditions. Overall urea electrolysis performance of the MoS₂ NPs/CoS₂ NTs: (e) LSV curves of the MoS₂ NPs/CoS₂ NTs (-,+) in the electrolyte with urea (1.0 M KOH + 0.5 M urea) or urine (1.0 M KOH + urine); (f) comparison of cell voltages at 10 mA cm⁻² of the MoS₂ NPs/CoS₂ NTs (-,+) under water splitting conditions and urea electrolysis conditions; (g) LSV curves of the MoS₂ NPs/CoS₂ NTs (-,+) and Pt/C (-) // RuO₂ (+) in the electrolyte with urea (1.0 M KOH + 0.5 M urea); (h) chronoamperometric curve of the MoS₂ NPs/CoS₂ NTs (-,+) and Pt/C (-) // RuO₂ (+); (i) Photograph of a urine electrolyzer using MoS₂ NPs/CoS₂ NTs as both cathode and anode.

consecutive water electrolysis based on MoS₂ NPs/CoS₂ NTs are observed in Fig. S25c. Fig. S25d shows that after 50 h stability testing, the cell voltages at 10 and 50 mA cm⁻² of the electrolyzer using MoS₂ NPs/CoS₂ NTs are slightly increased. The results confirm that the novel MoS₂ NPs/CoS₂ NTs material is an ideal candidate catalyst in overall water splitting applications requiring high performance and superior stability.

Considering that the MoS₂ NPs/CoS₂ NTs has excellent UOR and HER activity (Fig. 5a), the overall urea electrolyzer that relied on the MoS₂ NPs/CoS₂ NTs as both cathode and anode is assembled in this work as well. Initially, the performance of that electrolyzer is investigated by LSV measurement in the electrolyte with urea (1.0 M KOH + 0.5 M urea) or urine (1.0 M + urine). As seen in Fig. 5e, the LSV curve in the urine electrolyte is very close to that in the urea electrolyte, reconfirming the great potential of the MoS₂ NPs/CoS₂ NTs in real applications, especially for the treatment of urea-containing wastewater. The cell voltages at current densities of 10 and 50 mA cm⁻² are (1.4 and 1.69) and (1.47 and 1.7) V for the electrolyzer in the urine and urea electrolyte, respectively.

Clearly, the cell voltages at 50 mA cm⁻² for the urea electrolyzer are considerably lower than that for the water electrolyzer, as shown in Fig. 5f, testifying that the urea electrolyzer is more effective in terms of energy. Further, the overall urea electrolysis activity of the MoS₂ NPs/CoS₂ NTs is comparable to that of the Pt/C (-) // RuO₂ (+) commercial catalysts (Fig. 5g). The small cell voltage at 10 mA cm⁻² for urea electrolysis of the MoS₂ NPs/CoS₂ NTs is also superior to that of the transition metal-based bifunctional catalysts for urea electrolysis in the literature (Fig. S26a, and Table S5). The long-term durability of the urea electrolyzer based on the MoS₂ NPs/CoS₂ NTs electrodes was investigated under a standard potential of 1.7 V for 50 h. Fig. 5h shows that throughout the stability testing, the responding current density of MoS₂ NPs/CoS₂ NTs (-,+) based urea electrolyzer is more stable than that of the device based on commercial catalysts Pt/C (-) // RuO₂ (+).

Moreover, the LSV curve recorded after testing is almost like the initial one (Fig. S26b). Additionally, the cell voltages at 10 and 50 mA cm⁻² determined after long-term testing are negligibly enhanced, compared with those of the virgin material (Fig. S26c). Thus, the MoS₂ NPs/CoS₂ NTs-based urea electrolyzer is highly stable, even under successive operation. During electrochemical testing for the MoS₂ NPs/CoS₂ NTs-based device in urine electrolyte, many gas bubbles are released from the surface of the cathode and anode, as shown in Fig. 5i, corroborating that the MoS₂ NPs/CoS₂ NTs with its advantages of geometric and electronic structure is a highly efficient and stable electrocatalysts for urea electrolysis.

3.3. Density function theory calculations

It must be noted that clarifying the mechanism of electrochemical reactions taking place on the catalyst surface, as well as the surface charge distribution of catalysts, is necessary to explain the catalytic activity toward correctly predicting and constructing advanced electrocatalysts. In particular, regarding the OER, HER, and UOR electrocatalysts, their surface charge distribution needs to be paid more attention, owing to the important role of this feature in the reaction mechanism. Accordingly, we performed first-principles density functional theory (DFT) calculations to fully understand the Mott-Schottky effect, the alterations of electron density in the heterointerface, and the underlying reaction mechanisms to the MoS₂/CoS₂ catalytic systems. First, the projected density of states (PDOS) for isolated MoS₂(002) nanoparticle, CoS₂(112) surface, and MoS₂/CoS₂ heterostructure were calculated, as shown in Fig. 6a. Generally, the d-orbitals contribution to the density of states around the Fermi level is higher than that of the p-orbitals, indicating their dominant role in the catalytic activity of the MoS₂, CoS₂, and MoS₂/CoS₂ systems. The PDOS results also reveal the semiconductive nature of developed MoS₂ nanoparticle with a

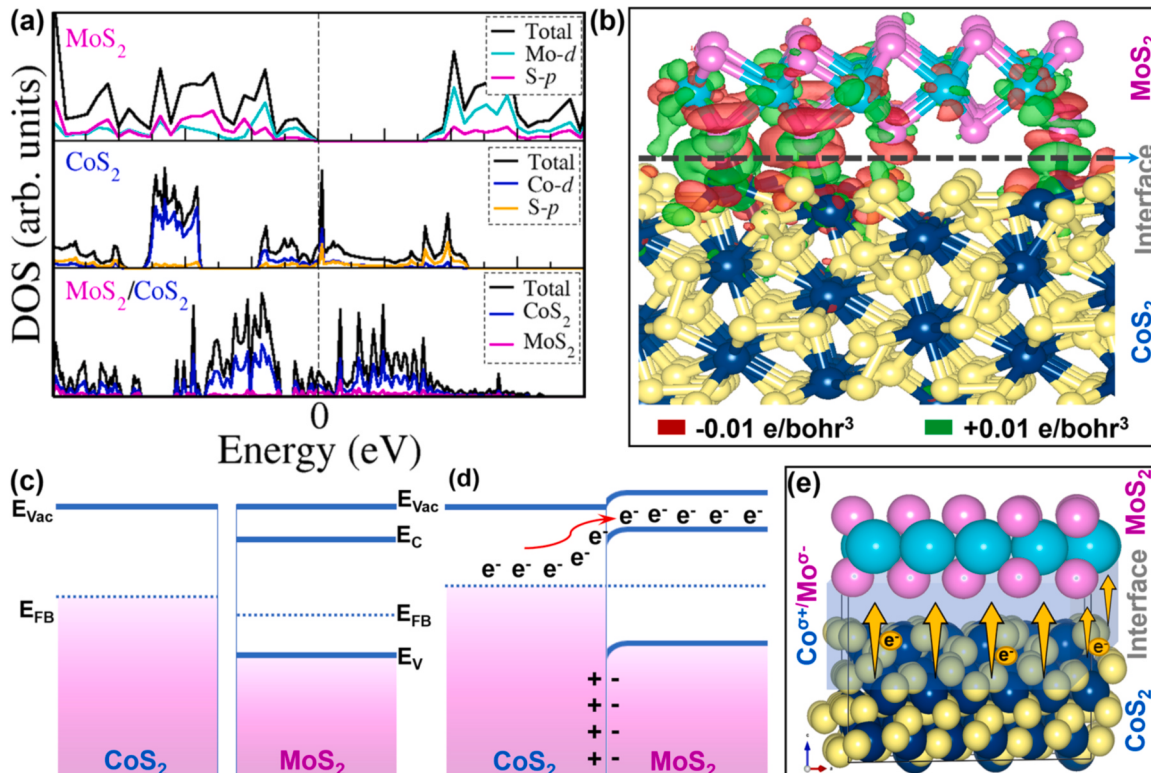


Fig. 6. (a) The DFT calculation PDOS for isolated MoS₂(002) nanoparticle, CoS₂(112) surface and MoS₂/CoS₂ heterointerface. (b) The charge density difference at the heterointerface of MoS₂/CoS₂. The energy band diagrams of semiconductive MoS₂ and metallic CoS₂ (c) before and (d) after the formation of Mott-Schottky interaction. (e) Schematic of the MoS₂/CoS₂ heterointerface depicting the electron transfer at the heterointerface. Color scheme: Mo, blue; S, pink (MoS₂); Co, dark blue; S, yellow (CoS₂).

sufficiently large band gap (1.65 eV) and the metallic properties of the isolated CoS_2 and $\text{MoS}_2/\text{CoS}_2$ heterostructure. In the $\text{MoS}_2/\text{CoS}_2$ Mott-Schottky heterojunction, the coupling of the valence band and conduction band within this structure is more favorable; this phenomenon is beneficial to the migration of electrons across the interband region, thus facilitating the reaction kinetics of the HER, OER, and UOR [58]. The decomposed PDOS of the $\text{MoS}_2/\text{CoS}_2$ heterostructure reveals hybridization between MoS_2 and CoS_2 , resulting from the newly formed Co-S bonds at the interface. The adhesion energy at the $\text{MoS}_2/\text{CoS}_2$ interface was predicted to be $-0.12 \text{ eV}/\text{\AA}^2$, which indicates that interface structure is thermodynamically stable for long-term operation.

To unravel the nature electron transfer across the $\text{MoS}_2/\text{CoS}_2$ heterointerface, differential charge density iso-surface contours were determined as shown Fig. 6b. Analysis of Fig. 6b shows that the space around the Mo species has a higher electron density in comparison with that around the Co species, corroborating the partial migration of electrons from CoS_2 to higher work function MoS_2 , which causes local electrophilic and nucleophilic regions at the interface of $\text{MoS}_2/\text{CoS}_2$ in

good agreement with the XPS results [27].

More interesting, the difference in Fermi level between the CoS_2 and MoS_2 cause migration of electrons across the heterointerface, resulting in tuning of electron density around the Co and Mo species (Fig. 6c-e), which has implications for their adsorption capacities towards reaction and intermediate species. Free energy calculations of the H- and O-containing intermediate species in the HER and OER were carried out for the isolated MoS_2 , CoS_2 , and $\text{MoS}_2/\text{CoS}_2$ heterostructure to evaluate their adsorption abilities for these key intermediates. The top and side views of the crystal structures of MoS_2 , CoS_2 , and $\text{MoS}_2/\text{CoS}_2$ are shown in Fig. 7a. The corresponding H adsorption sites for these systems are illustrated in the Inset of Fig. 7b-d. Taking Mo and S species as the adsorption sites for MoS_2 , Co and S species as the adsorption sites for CoS_2 , and Mo, Co, and S species as the adsorption sites for $\text{MoS}_2/\text{CoS}_2$, the difference of Gibbs free energy for adsorbed hydrogen (ΔG_{H^*}) was calculated for the MoS_2 , CoS_2 , and $\text{MoS}_2/\text{CoS}_2$, as shown in Fig. 7b-d, respectively. The ΔG_{H^*} values of the Mo and S sites for MoS_2 are found to be -0.32 and 0.59 eV, respectively, which are rather far away from the

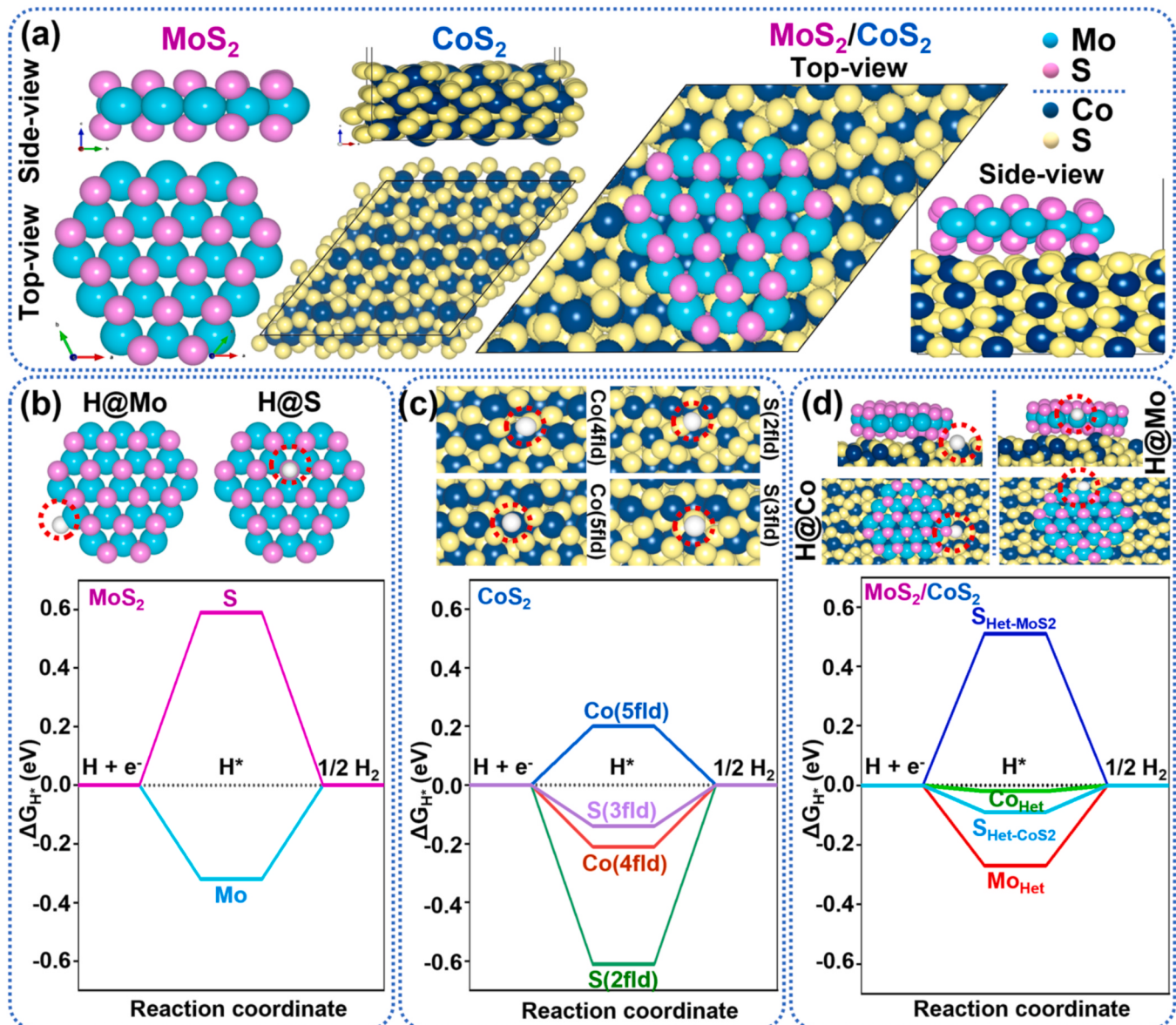


Fig. 7. (a) Optimized crystal structures of MoS_2 (002) nanoparticle, CoS_2 (112) and $\text{MoS}_2/\text{CoS}_2$ heterointerface. (b)-(d) The Gibbs free energy diagram of HER at different H adsorption sites on the surface of MoS_2 , CoS_2 , and $\text{MoS}_2/\text{CoS}_2$, respectively. Inset of (b)-(d): the considered H adsorption sites for MoS_2 , CoS_2 , and $\text{MoS}_2/\text{CoS}_2$, respectively. Color scheme: Mo, blue; S, pink (MoS_2); Co, dark blue; S, yellow (CoS_2).

criterion value of 0 eV, suggesting their moderate HER behavior (Fig. 7b). Regarding the CoS₂ system, we calculated ΔG_{H^*} for two different kinds of Co and S sites, including Co site with four adjacent S atoms (namely Co(4fld)), Co site with five adjacent S atoms (namely Co(5fld)), S site with two adjacent Co atoms (namely S(2fld)), and S site with three adjacent Co atoms (namely S(3fld)). As shown in Fig. 7c, the negative ΔG_{H^*} values of the Co(4fld) site (-0.21 eV), S(2fld) site (-0.61 eV), and S(3fld) site (-0.14 eV) indicate that these sites deliver strong adsorption energy for H intermediate, while the positive ΔG_{H^*} value of the Co(5fld) site (0.20 eV) suggests it's too weak binding energy toward the H intermediate, causing difficult adsorption or desorption of H intermediates on these sites and thereby bringing speed-down of the HER kinetics. This demonstrates that CoS₂ alone does not offer much promise as an electrocatalyst for the HER, in line with the experimental results.

Remarkably, the optimal ΔG_{H^*} values of the Mo (-0.27 eV) and S

(0.51 eV) sites belonging to the MoS₂ component, and Co (-0.02 eV), and S (-0.09 eV) sites belonging to the CoS₂ component for the MoS₂/CoS₂ heterojunction (Fig. 7d) confirm that the formation of Mott-Schottky interfacial interaction between the MoS₂ and CoS₂ favors the adsorption of H intermediates, which can facilitate the HER kinetics and favor the performance of the HER process.

Turning our attention to water adsorption, which directly affects the kinetics of catalytic reactions, the adsorption energy of water molecules on the MoS₂, CoS₂, and MoS₂/CoS₂ surface was also calculated. Fig. 8a presents theoretical models of adsorbed H₂O on Mo-top and Mo-edge sites of MoS₂, Co site of CoS₂, and Co and Mo sites of MoS₂/CoS₂ Mott-Schottky heterojunction. The adsorption energies are found to be -0.15, -0.95, -0.52, -0.71, and -1.02 eV for Mo-top and Mo-edge sites of MoS₂, Co site of CoS₂, and Co and Mo sites of MoS₂/CoS₂, respectively. The adsorption energies are found to be -0.15, and -0.95 eV for Mo-top and Mo-edge sites of MoS₂, respectively. Also, we

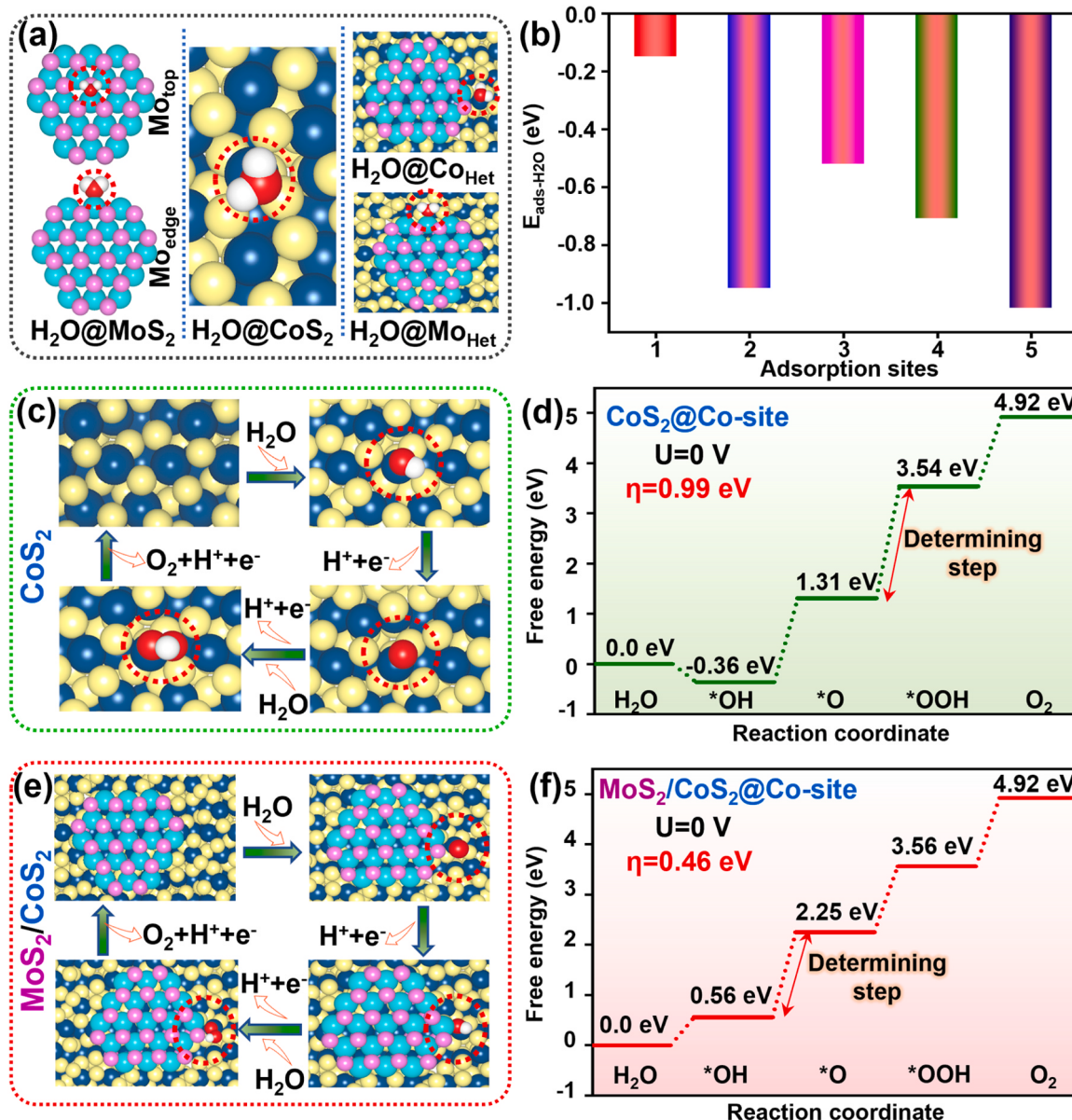


Fig. 8. (a) The considered water adsorption sites for MoS₂, CoS₂, and MoS₂/CoS₂. (b) Water adsorption energy on the MoS₂, CoS₂, and MoS₂/CoS₂ systems (Adsorption sites: 1, Mo-top (MoS₂); 2, Mo-edge (MoS₂); 3, Co (CoS₂); 4, Co (MoS₂/CoS₂); and 5, Mo (MoS₂/CoS₂)). (c) The proposed four proton-transfer mechanism of OER in alkaline conditions at Co binding site on the surface of CoS₂ alone, and (d) the corresponding Gibbs free energy diagram of OER. (e) The proposed four proton-transfer mechanism of OER in alkaline conditions at Co binding site on the surface of MoS₂/CoS₂, and (f) the corresponding Gibbs free energy diagram of OER. Color scheme: Mo, blue; S, pink (MoS₂); Co, dark blue; S, yellow (CoS₂).

calculated that the adsorption energy of a water molecule on Co site of CoS_2 is -0.52 eV. Importantly, after integrating MoS_2 and CoS_2 constituents to form Mott-Schottky heterojunction, the water adsorption energy on Mo site (-1.02 eV) and Co site (-0.71 eV) of $\text{MoS}_2/\text{CoS}_2$ is lower than those on Mo sites of MoS_2 alone and Co site of CoS_2 alone, respectively, meaning that the adsorption of water molecule on the $\text{MoS}_2/\text{CoS}_2$ heterojunction is more thermodynamically favorable than those on MoS_2 and CoS_2 [43,59]. Such strong binding ability of our heterostructure for the water molecules is conducive to the catalytic performance in alkaline conditions. Regarding the OER, the difference of Gibbs free energies for O-containing intermediates (ΔG_{M^*} ; $\text{M} = \text{OH}, \text{O}$, and OOH) was also determined via DFT calculations. Generally, the alkaline OER process is governed by the four proton-transfer mechanism proposed by Norskow [58], and its efficiency mostly depends on the adsorption energy of ${}^*\text{OH}$, ${}^*\text{O}$, and ${}^*\text{OOH}$ species on the catalyst surface. Herein, we initially calculated ΔG_{M^*} on the Co site of the CoS_2 system. The proposed adsorption process of these intermediate species on the Co site of CoS_2 surface under alkaline OER is illustrated in Fig. 8c, while the corresponding free energy diagram is shown in Fig. 8d. The ΔG_{OH^*} value of the Co site on CoS_2 is very low, at around -0.36 eV, far away from the criterion value of 1.23 eV, suggesting that the bond between Co and ${}^*\text{O}$ intermediate is very strong, and is thus unfavorable for the entire reaction kinetics of the OER. Indeed, the theoretical overpotential for OER taking place on the Co site of CoS_2 is calculated to be 0.99 eV, which is a relatively high value, indicating that the catalytic activity of CoS_2 for OER is not very desirable.

On the other hand, because of its highest step distance, the rate-determining step for CoS_2 is determined to be the ${}^*\text{OOH}$ formation. In contrast, after combining with the semiconductive MoS_2 to form the $\text{MoS}_2/\text{CoS}_2$ Mott-Schottky heterojunction, the regulation of electronic structure at the heterointerface caused a positive influence on the energy barriers of intermediate adsorption to be demonstrated. Fig. 8e and f show the proposed adsorption process of O-related intermediate species on the Co site of $\text{MoS}_2/\text{CoS}_2$ surface under alkaline OER and the corresponding free energy diagram, respectively. The ΔG_{OH^*} value of the Co site (0.56 eV) in the heterointerface of $\text{MoS}_2/\text{CoS}_2$ approaches the ideal value (1.23 eV), suggesting the optimal binding energy strength between Co and ${}^*\text{OH}$. Thus, the chemical coupling effect between MoS_2 and CoS_2 brings about an optimal free energy for the adsorbed OER intermediates to the MoS_2 NPs/ CoS_2 NTs, which facilitates the OER kinetics, and leads to remarkable reduction in the overpotential to 0.46 eV. The step of ${}^*\text{O}$ formation is recognized as the rate-determining step of the OER process occurring over the Co site of $\text{MoS}_2/\text{CoS}_2$ interface. Similarly, we also calculated the ΔG_{M^*} on the S site of the MoS_2 system (Fig. S27) and the result shows that the MoS_2 is not suitable for the OER with a high theoretical overpotential of 1.55 eV. Furthermore, to clarify the role of the in-situ oxidized CoOOH species formed over the surface of MoS_2 NPs/ CoS_2 NTs during the OER catalysis as mentioned above, we have investigated the OER on the two-dimensional (2D) CoOOH surface of the $\text{MoS}_2/\text{CoOOH}/\text{CoS}_2$ heterointerface catalyst. As shown in Fig. S28, two different active sites Co–O (denoted as A) and Co–OH (denoted as B) were explored on the 2D $\text{CoOOH}(001)$ surface. When the reaction starts at the A site (Co–O), the formation of ${}^*\text{OOH}$ is the initial step, and when it starts from the B (Co–OH) site, the deprotonation of hydroxyl groups is the initial step. On both active sites, the following intermediates are considered: oxo (${}^*\text{O}$), hydroxo (${}^*\text{OH}$), hydroperoxo (${}^*\text{OOH}$), and superoxo (${}^*\text{O}_2$), where $*$ represents either A- or B-site. Shown in Figs. S29a and b are the optimized structures of the reaction intermediates involved in the lowest overpotential OER mechanisms on the A and B active sites, respectively. The standard Gibbs free energy profiles for the OER on the A and B active sites are depicted in Figs. S30a and b, respectively. The energy barriers for the four electrochemical steps at the A site (Co–O) are 1.62 , 0.89 , 0.82 , and 1.44 eV, respectively, with the rate-determining step predicted to be the formation of the ${}^*\text{OOH}$ intermediate with an energy barrier of 1.62 eV and a theoretical overpotential (1.62 – 1.23 V) of 0.43 V. At the B

(Co–OH) site, the energy barriers for the four electrochemical steps are 1.52 , 1.61 , 1.12 , and 0.56 eV, respectively, with the rate-determining step predicted to be a nucleophilic attack of OH^- on Co–OH species to form ${}^*\text{OOH}$ intermediate. The theoretical overpotential is predicted at 0.38 V (1.61 – 1.23 V). The findings, accompanied by the very small theoretical overpotential of both A and B sites argue that the Co–O and Co–OH binding sites on the 2D CoOOH surface of the $\text{MoS}_2/\text{CoOOH}/\text{CoS}_2$ have favorable reaction kinetics and excellent OER activity, corroborating that in-situ oxidized CoOOH species serve as the real active sites for the OER catalysis. Moreover, the desorption energy of O_2 from the 2D CoOOH at the A and B sites is calculated at 0.15 and 0.11 eV, respectively, indicating that the B-site is catalytically more active for OER than the A-site.

4. Conclusions

In summary, we have demonstrated an advanced Mott-Schottky heterogeneous electrocatalyst consisting of MoS_2 NPs/ CoS_2 NTs grown on a conductive CC substrate. Here, CoS_2 with the morphology feature of nanotube arrays acts as a low-resistance path for charge/mass transfer, while MoS_2 NPs with ultrasmall property provide more active sites, as compared to the other bulk morphologies reported elsewhere. Importantly, the Mott-Schottky interaction formed at the heterointerface between MoS_2 and CoS_2 creates optimal energy adsorption for intermediate species via adjusting the electronic structure of both MoS_2 and CoS_2 , thus accelerating the HER, OER, and UOR reaction kinetics. Encouraged by the promising catalytic behaviors for HER, OER, and UOR, the advanced MoS_2 NPs/ CoS_2 NTs catalyst shows excellent catalytic performance for overall water and urea electrolysis. The assembled water and urea electrolyzers using MoS_2 NPs/ CoS_2 NTs electrodes require small cell voltage of 1.65 and 1.4 V to achieve a current density of 10 mA cm^{-2} , respectively, which values are superior to those of the multifunctional electrocatalysts based on earth-abundant transition metals demonstrated by previous works. The DFT calculations shed light on the underlying reaction mechanisms and synergistic effects between MoS_2 and CoS_2 in the $\text{MoS}_2/\text{CoS}_2$ Mott-Schottky heterojunction that resulted in their superior electrocatalytic performance. Our study with excellent experimental results and obvious theoretical calculations contributes to the exploration of efficient electrocatalysts for energy conversion techniques, especially for the future green H_2 energy industry.

CRediT authorship contribution statement

Thi Luu Luyen Doan: Conceptualization, Methodology, Writing – original draft, Validation, Visualization, Project administration. **Dinh Chuong Nguyen:** Methodology, Writing – reviewing and Editing. **Kyoungin Kang:** Investigation, Formal analysis. **Anusha Ponnusamy:** Methodology, Investigation. **Henry I. Eya:** Density-functional theory calculation, Writing – reviewing, and Editing. **Cheol Sang Kim:** Conceptualization, Data curation, Writing – reviewing and editing, Supervision. **Chan Hee Park:** Conceptualization, Writing – reviewing and editing, Supervision, Project administration. T.L.D. was involved in the discovery of the catalyst. **T.L.D., D.C.N., K.G.K., A.P., C.S.K., and C.H.P.** designed and synthesized the catalysts. **T.L.D., D.C.N., K.G.K., and A.P.**, Performed the experiments. **T.L.D., H.I.E., and N.Y.D** performed theoretical calculations, and All of the authors analyzed the data and designed the experiments.

Declaration of Competing Interest

The authors declare that they have no known competing financial interests or personal relationships that could have appeared to influence the work reported in this paper.

Data availability

Data will be made available on request.

Acknowledgments

This study was supported by the National Research Foundation of Korea (NRF) grant funded by the Korean Ministry of Education (2021R1I1A1A01060737) and the Regional Leading Research Center Program (2019R1A5A8080326) through the National Research Foundation funded by the Ministry of Science and ICT of Republic of Korea. N.Y.D and H.I.E acknowledge Seed Grant support from the Penn State Institute for Computational and Data Sciences and from the Institutes of Energy and the Environment. Computations for this research were performed on the Pennsylvania State University's Institute for Computational and Data Sciences' Roar supercomputer.

Appendix A. Supporting information

Supplementary data associated with this article can be found in the online version at [doi:10.1016/j.apcatb.2023.123295](https://doi.org/10.1016/j.apcatb.2023.123295).

References

- [1] Y. Liu, X. He, D. Hanlon, A. Harvey, U. Khan, Y. Li, J.N. Coleman, Electrical, mechanical, and capacity percolation leads to high-performance MoS₂/nanotube composite lithium ion battery electrodes, *ACS Nano* 10 (2016) 5980–5990, <https://doi.org/10.1021/acsnano.6b01505>.
- [2] N.D. Chuong, T.D. Thanh, N.H. Kim, J.H. Lee, Hierarchical heterostructures of ultrasmall Fe₂O₃-encapsulated MoS₂/N-graphene as an effective catalyst for oxygen reduction reaction, *ACS Appl. Mater. Interfaces* 10 (2018) 24523–24532, <https://doi.org/10.1021/acsmami.8b06485>.
- [3] X. Zhu, D.C. Nguyen, S. Prabhakaran, D.H. Kim, N.H. Kim, J.H. Lee, Activating catalytic behavior of binary transition metal sulfide-shelled carbon nanotubes by iridium incorporation toward efficient overall water splitting, *Mater. Today Nano* 21 (2023), 100296, <https://doi.org/10.1016/j.mtnano.2022.100296>.
- [4] M. Wang, L. Zhang, Y. He, H. Zhu, Recent advances in transition-metal-sulfide-based bifunctional electrocatalysts for overall water splitting, *J. Mater. Chem. A* 9 (2021) 5320–5363, <https://doi.org/10.1039/DOTA121152E>.
- [5] T.L. Luyen Doan, D.T. Tran, D.C. Nguyen, H. Tuan Le, N.H. Kim, J.H. Lee, Hierarchical three-dimensional framework interface assembled from oxygen-doped cobalt phosphide layer-shelled metal nanowires for efficient electrocatalytic water splitting, *Appl. Catal. B Environ.* 261 (2020), 118268, <https://doi.org/10.1016/j.apcatb.2019.118268>.
- [6] F. Niu, D. Wang, F. Li, Y. Liu, S. Shen, T.J. Meyer, Hybrid photoelectrochemical water splitting systems: from interface design to system assembly, *Adv. Energy Mater.* 10 (2020), 1900399, <https://doi.org/10.1002/aenm.201900399>.
- [7] T.L.L. Doan, D.T. Tran, D.C. Nguyen, D.H. Kim, N.H. Kim, J.H. Lee, Rational engineering Co_xO_y nanosheets via phosphorous and sulfur dual-coupling for enhancing water splitting and Zn–Air battery, *Adv. Funct. Mater.* 31 (2021), 2007822, <https://doi.org/10.1002/adfm.202007822>.
- [8] D.C. Nguyen, T.L. Luyen Doan, S. Prabhakaran, D.T. Tran, D.H. Kim, J.H. Lee, N. H. Kim, Hierarchical Co and Nb dual-doped MoS₂ nanosheets shelled micro-TiO₂ hollow spheres as effective multifunctional electrocatalysts for HER, OER, and ORR, *Nano Energy* 82 (2021), 105750, <https://doi.org/10.1016/j.nano.2021.105750>.
- [9] S. Sultan, J.N. Tiwari, A.N. Singh, S. Zhumagali, M. Ha, C.W. Myung, P. Thangavel, K.S. Kim, Single atoms and clusters based nanomaterials for hydrogen evolution, oxygen evolution reactions, and full water splitting, *Adv. Energy Mater.* 9 (2019), 1900624, <https://doi.org/10.1002/aenm.201900624>.
- [10] S.A. Patil, S. Cho, Y. Jo, N.K. Shrestha, H. Kim, H. Im, Bimetallic Ni-Co@hexacyano nano-frameworks anchored on carbon nanotubes for highly efficient overall water splitting and urea decontamination, *Chem. Eng. J.* 426 (2021), 130773, <https://doi.org/10.1016/j.cej.2021.130773>.
- [11] D.C. Nguyen, T.L.L. Doan, S. Prabhakaran, D.H. Kim, N.H. Kim, J.H. Lee, Rh single atoms/clusters confined in metal sulfide/oxide nanotubes as advanced multifunctional catalysts for green and energy-saving hydrogen productions, *Appl. Catal. B Environ.* 313 (2022), 121430, <https://doi.org/10.1016/j.apcatb.2022.121430>.
- [12] D.C. Nguyen, T.L.L. Doan, S. Prabhakaran, D.H. Kim, N.H. Kim, J.H. Lee, Rational construction of Au@Co₂N_{0.67} nanodots-interspersed 3D interconnected N-graphene hollow sphere network for efficient water splitting and Zn-air battery, *Nano Energy* 89 (2021), 106420, <https://doi.org/10.1016/j.nanoen.2021.106420>.
- [13] H. Sun, W. Zhang, J.-G. Li, Z. Li, X. Ao, K.-H. Xue, K.K. Ostrikov, J. Tang, C. Wang, Rh-engineered ultrathin NiFe-LDH nanosheets enable highly-efficient overall water splitting and urea electrolysis, *Appl. Catal. B Environ.* 284 (2021), 119740, <https://doi.org/10.1016/j.apcatb.2020.119740>.
- [14] S. Singh, D.C. Nguyen, N.H. Kim, J.H. Lee, Interface engineering induced electrocatalytic behavior in core-shelled CNTs@NiP₂/NbP heterostructure for highly efficient overall water splitting, *Chem. Eng. J.* 442 (2022), 136120, <https://doi.org/10.1016/j.cej.2022.136120>.
- [15] D.C. Nguyen, D.T. Tran, T.L. Luyen Doan, N.H. Kim, J.H. Lee, Constructing Mo_x@Mn_y heteronanoparticle-supported mesoporous N,P-codoped graphene for boosting oxygen reduction and oxygen evolution reaction, *Chem. Mater.* 31 (2019) 2892–2904, <https://doi.org/10.1021/acs.chemmater.9b00071>.
- [16] T.L.L. Doan, D.C. Nguyen, P.M. Bacirhonde, A.S. Yasin, A.I. Rezk, N.Y. Dzade, C. S. Kim, C.H. Park, Atomic dispersion of Rh on interconnected Mo₂C nanosheet network intimately embedded in 3D Ni_xMo_y nanorod arrays for pH-universal hydrogen evolution, *Energy Environ. Mater.* 0 (2023) 1–15, <https://doi.org/10.1002/eem.212407>.
- [17] D.C. Nguyen, D.T. Tran, T.L.L. Doan, D.H. Kim, N.H. Kim, J.H. Lee, Rational design of core@shell structured Co_x@Cu₂MoS₄ hybridized MoS₂/N,S-codoped graphene as advanced electrocatalyst for water splitting and Zn-Air battery, *Adv. Energy Mater.* 10 (2020), 1903289, <https://doi.org/10.1002/aenm.201903289>.
- [18] S. Shit, S. Chhetri, S. Bolar, N.C. Murmu, W. Jang, H. Koo, T. Kuila, Hierarchical cobalt sulfide/molybdenum sulfide heterostructure as bifunctional electrocatalyst towards overall water splitting, *ChemElectroChem* 6 (2019) 430–438, <https://doi.org/10.1002/celec.201801343>.
- [19] Z. Shi, X. Qi, Z. Zhang, Y. Song, J. Zhang, C. Guo, W. Xu, K. Liu, Z. Zhu, Interface engineering of cobalt–sulfide–selenium core–shell nanostructures as bifunctional electrocatalysts toward overall water splitting, *Nanoscale* 13 (2021) 6890–6901, <https://doi.org/10.1039/DINR00987G>.
- [20] F. Li, R. Xu, Y. Li, F. Liang, D. Zhang, W.-F. Fu, X.-J. Lv, N-doped carbon coated NiCo₂S₄ hollow nanotube as bifunctional electrocatalyst for overall water splitting, *Carbon N.* 145 (2019) 521–528, <https://doi.org/10.1016/j.carbon.2019.01.065>.
- [21] X. Han, X. Wu, Y. Deng, J. Liu, J. Lu, C. Zhong, W. Hu, Ultrafine Pt nanoparticle-decorated pyrite-type CoS₂ nanosheet arrays coated on carbon cloth as a bifunctional electrode for overall water splitting, *Adv. Energy Mater.* 8 (2018), 1800935, <https://doi.org/10.1002/aenm.201800935>.
- [22] Z. Xie, H. Tang, Y. Wang, MOF-derived Ni-doped CoS₂ grown on carbon fiber paper for efficient oxygen evolution reaction, *ChemElectroChem* 6 (2019) 1206–1212, <https://doi.org/10.1002/celec.201801106>.
- [23] Y. Jiang, S. Gao, J. Liu, G. Xu, Q. Jia, F. Chen, X. Song, Ti-Mesh supported porous CoS₂ nanosheet self-interconnected networks with high oxidation states for efficient hydrogen production via urea electrolysis, *Nanoscale* 12 (2020) 11573–11581, <https://doi.org/10.1039/DONR02058C>.
- [24] T.L.L. Doan, D.C. Nguyen, S. Prabhakaran, D.H. Kim, D.T. Tran, N.H. Kim, J.H. Lee, Single-atom Co-decorated MoS₂ nanosheets assembled on metal nitride nanorod arrays as an efficient bifunctional electrocatalyst for pH-universal water splitting, *Adv. Funct. Mater.* 31 (2021), 2100233, <https://doi.org/10.1002/adfm.202100233>.
- [25] Q. Wen, K. Yang, D. Huang, G. Cheng, X. Ai, Y. Liu, J. Fang, H. Li, L. Yu, T. Zhai, Schottky heterojunction nanosheet array achieving high-current-density oxygen evolution for industrial water splitting electrolyzers, *Adv. Energy Mater.* 11 (2021), 2102353, <https://doi.org/10.1002/aenm.202102353>.
- [26] T.L.L. Doan, D.C. Nguyen, R. Amaral, N.Y. Dzade, C.S. Kim, C.H. Park, Rationally designed NiS₂-Mn_xMoS₂ hybridized 3D hollow N-Gr microsphere framework-modified celgard separator for highly efficient Li-S batteries, *Appl. Catal. B Environ.* 319 (2022), 121934, <https://doi.org/10.1016/j.apcatb.2022.121934>.
- [27] C. Li, Y. Liu, Z. Zhuo, H. Ju, D. Li, Y. Guo, X. Wu, H. Li, T. Zhai, Local charge distribution engineered by schottky heterojunctions toward urea electrolysis, *Adv. Energy Mater.* 8 (2018), 1801775, <https://doi.org/10.1002/aenm.201801775>.
- [28] V. Ganeshan, J. Kim, Multi-shelled CoS₂–MoS₂ hollow spheres as efficient bifunctional electrocatalysts for overall water splitting, *Int. J. Hydrol. Energy* 45 (2020) 13290–13299, <https://doi.org/10.1016/j.ijhydene.2020.03.045>.
- [29] Q. Wang, Z.-Y. Tian, W.-J. Cui, N. Hu, S.-M. Zhang, Y.-Y. Ma, Z.-G. Han, Hierarchical flower-like CoS₂-MoS₂ heterostructure spheres as efficient bifunctional electrocatalyst for overall water splitting, *Int. J. Hydrol. Energy* 47 (2022) 12629–12641, <https://doi.org/10.1016/j.ijhydene.2022.02.024>.
- [30] B. Zhang, Z. Qi, Z. Wu, Y.H. Lui, T.-H. Kim, X. Tang, L. Zhou, W. Huang, S. Hu, Defect-rich 2D material networks for advanced oxygen evolution catalysts, *ACS Energy Lett.* 4 (2019) 328–336, <https://doi.org/10.1021/acsenergylett.8b02243>.
- [31] Z. Yu, Y. Bai, S. Zhang, Y. Liu, N. Zhang, K. Sun, MOF-directed templating synthesis of hollow nickel–cobalt sulfide with enhanced electrocatalytic activity for oxygen evolution, *Int. J. Hydrol. Energy* 43 (2018) 8815–8823, <https://doi.org/10.1016/j.ijhydene.2018.03.154>.
- [32] C. Guan, X. Liu, A.M. Elshahawy, H. Zhang, H. Wu, S.J. Pennycook, J. Wang, Metal–organic framework derived hollow CoS₂ nanotube arrays: an efficient bifunctional electrocatalyst for overall water splitting, *Nanoscale Horiz.* 2 (2017) 342–348, <https://doi.org/10.1039/C7NH00079K>.
- [33] J. Qin, J. Barrio, G. Peng, J. Tzadikov, L. Abisdris, M. Volokh, M. Shalom, Direct growth of uniform carbon nitride layers with extended optical absorption towards efficient water-splitting photoanodes, *Nat. Commun.* 11 (2020), 4701, <https://doi.org/10.1038/s41467-020-18535-0>.
- [34] Y.Z. Wang, M. Yang, Y. Ding, N. Li, L. Yu, Recent advances in complex hollow electrocatalysts for water splitting, *Adv. Funct. Mater.* 32 (2022), 2108681, <https://doi.org/10.1002/adfm.202108681>.
- [35] Y. Li, Y.-Q. Zhu, W. Xin, S. Hong, X. Zhao, H. Yan, S. Xu, Interlayer confinement synthesis of Ir nanodots/dual carbon as an electrocatalyst for overall water splitting, *J. Mater. Chem. A* 9 (2021) 4176–4183, <https://doi.org/10.1039/DOTA09358K>.
- [36] P. Wang, Y. Luo, G. Zhang, M. Wu, Z. Chen, S. Sun, Z. Shi, MnO_x-decorated nickel–iron phosphides nanosheets: interface modifications for Robust overall water splitting at ultra-high current densities, *Small* 18 (2022), 2105803, <https://doi.org/10.1002/smll.202105803>.

- [37] H. Hu, W. Ding, G. Sun, Z. Yao, Novel highly active and stable alumina-supported cobalt nitride catalyst for dry reforming of methane, *Appl. Surf. Sci.* 606 (2022), 154802, <https://doi.org/10.1016/j.apsusc.2022.154802>.
- [38] G. Fang, J. Zhou, C. Liang, A. Pan, C. Zhang, Y. Tang, X. Tan, J. Liu, S. Liang, MOFs nanosheets derived porous metal oxide-coated three-dimensional substrates for lithium-ion battery applications, *Nano Energy* 26 (2016) 57–65, <https://doi.org/10.1016/j.nanoen.2016.05.009>.
- [39] C. Guan, X. Liu, W. Ren, X. Li, C. Cheng, J. Wang, Rational design of metal-organic framework derived hollow NiCo₂O₄ arrays for flexible supercapacitor and electrocatalysis, *Adv. Energy Mater.* 7 (2017) 1602391, <https://doi.org/10.1002/aenm.201602391>.
- [40] D. Wang, Y. Liu, L. Liu, D. Shan, G. Shen, S. Peng, H. Zhang, X. Wang, Biomimetic three-dimensional multilevel nanoarray electrodes with superaerobicity as efficient bifunctional catalysts for electrochemical water splitting, *Nano Res.* (2023), <https://doi.org/10.1007/s12274-022-5373-4>.
- [41] S.R. Kadam, D.J. Late, R.P. Panmand, M.V. Kulkarni, L.K. Nikam, S.W. Gosavi, C. J. Park, B.B. Kale, Nanostructured 2D MoS₂ honeycomb and hierarchical 3D CdMoS₄ marigold nanoflowers for hydrogen production under solar light, *J. Mater. Chem. A* 3 (2015) 21233–21243, <https://doi.org/10.1039/C5TA04617C>.
- [42] P. Liu, J. Yan, J. Mao, J. Li, D. Liang, W. Song, In-plane intergrowth CoS₂/MoS₂ nanosheets: binary metal-organic framework evolution and efficient alkaline HER electrocatalysis, *J. Mater. Chem. A* 8 (2020) 11435–11441, <https://doi.org/10.1039/D0TA00897D>.
- [43] L. Yang, R. Liu, L. Jiao, Electronic redistribution: construction and modulation of interface engineering on CoP for enhancing overall water splitting, *Adv. Funct. Mater.* 30 (2020), 1909618, <https://doi.org/10.1002/adfm.201909618>.
- [44] Y. Guo, J. Tang, J. Henzie, B. Jiang, W. Xia, T. Chen, Y. Bando, Y.-M. Kang, M.S. A. Hossain, Y. Sugahara, Y. Yamauchi, Mesoporous iron-doped MoS₂/CoMo₂S₄ heterostructures through organic–metal cooperative interactions on spherical micelles for electrochemical water splitting, *ACS Nano* 14 (2020) 4141–4152, <https://doi.org/10.1021/acsnano.9b08904>.
- [45] X. Yang, R. Sun, P. Zan, L. Zhao, J. Lian, Growth of vertically aligned Co₃S₄/CoMo₂S₄ ultrathin nanosheets on reduced graphene oxide as a high-performance supercapacitor electrode, *J. Mater. Chem. A* 4 (2016) 18857–18867, <https://doi.org/10.1039/C6TA07898B>.
- [46] X. Peng, Y. Yan, S. Xiong, Y. Miao, J. Wen, Z. Liu, B. Gao, L. Hu, P.K. Chu, Se-NiSe₂ hybrid nanosheet arrays with self-regulated elemental Se for efficient alkaline water splitting, *J. Mater. Sci. Technol.* 118 (2022) 136–143, <https://doi.org/10.1016/j.jmst.2021.12.022>.
- [47] W. Zhang, N. Han, J. Luo, X. Han, S. Feng, W. Guo, S. Xie, Z. Zhou, P. Subramanian, K. Wan, J. Arbiol, C. Zhang, S. Liu, M. Xu, X. Zhang, J. Fransaer, Critical role of phosphorus in hollow structures cobalt-based phosphides as bifunctional catalysts for water splitting, *Small* 18 (2022), 2103561, <https://doi.org/10.1002/smll.202103561>.
- [48] S. Lin, Y. Yu, D. Sun, F. Meng, W. Chu, L. Huang, J. Ren, Q. Su, S. Ma, B. Xu, FeNi₂P three-dimensional oriented nanosheet array bifunctional catalysts with better full water splitting performance than the full noble metal catalysts, *J. Colloid Interface Sci.* 608 (2022) 2192–2202, <https://doi.org/10.1016/j.jcis.2021.09.166>.
- [49] X. Wang, G. Huang, Z. Pan, S. Kang, S. Ma, P.K. Shen, J. Zhu, One-pot synthesis of Mn₂P-Mn₂O₃ heterogeneous nanoparticles in a P, N -doped three-dimensional porous carbon framework as a highly efficient bifunctional electrocatalyst for overall water splitting, *Chem. Eng. J.* 428 (2022), 131190, <https://doi.org/10.1016/j.cej.2021.131190>.
- [50] X. Gao, H. Zhang, Q. Li, X. Yu, Z. Hong, X. Zhang, C. Liang, Z. Lin, Hierarchical NiCo₂O₄ hollow microcuboids as bifunctional electrocatalysts for overall water-splitting, *Angew. Chem. Int. Ed.* 55 (2016) 6290–6294, <https://doi.org/10.1002/anie.201600525>.
- [51] F. Meng, Y. Yu, D. Sun, L. Li, S. Lin, L. Huang, W. Chu, S. Ma, B. Xu, Three-dimensional flower-like WP₂ nanowire arrays grown on Ni foam for full water splitting, *Appl. Surf. Sci.* 546 (2021), 148926, <https://doi.org/10.1016/j.apsusc.2021.148926>.
- [52] R. Li, B. Hu, T. Yu, H. Chen, Y. Wang, S. Song, Insights into correlation among surface-structure-activity of cobalt-derived Pre-catalyst for oxygen evolution reaction, *Adv. Sci.* 7 (2020), 1902830, <https://doi.org/10.1002/advs.201902830>.
- [53] Z. Yin, X. Liu, S. Chen, H. Xie, L. Gao, A. Liu, T. Ma, Y. Li, Interface engineering of the MoS₂/NiS₂/CoS₂ nanotube as a highly efficient bifunctional electrocatalyst for overall water splitting, *Mater. Today Nano* 17 (2022), 100156, <https://doi.org/10.1016/j.mtnano.2021.100156>.
- [54] B. Zhang, J. Shan, W. Wang, P. Tsakaras, Y. Li, Oxygen Vacancy and Core–Shell Heterojunction Engineering of Anemone-Like CoP@CoOOH Bifunctional Electrocatalyst for Efficient Overall Water Splitting, *Small* 18 (2022), 2106012, <https://doi.org/10.1002/smll.202106012>.
- [55] H. Chu, P. Feng, B. Jin, G. Ye, S. Cui, M. Zheng, G.-X. Zhang, M. Yang, In-situ release of phosphorus combined with rapid surface reconstruction for Co–Ni bimetallic phosphides boosting efficient overall water splitting, *Chem. Eng. J.* 433 (2022), 133523, <https://doi.org/10.1016/j.cej.2021.133523>.
- [56] W. Shi, R. Ding, X. Li, Q. Xu, E. Liu, Enhanced performance and electrocatalytic kinetics of Ni-Mo/graphene nanocatalysts towards alkaline urea oxidation reaction, *Electrochim. Acta* 242 (2017) 247–259, <https://doi.org/10.1016/j.electacta.2017.05.002>.
- [57] T. Liu, D. Liu, F. Qu, D. Wang, L. Zhang, R. Ge, S. Hao, Y. Ma, G. Du, A.M. Asiri, L. Chen, X. Sun, Enhanced electrocatalysis for energy-efficient hydrogen production over CoP catalyst with nonelectroactive Zn as a promoter, *Adv. Energy Mater.* 7 (2017), 1700020, <https://doi.org/10.1002/aenm.201700020>.
- [58] L. Wang, X. Duan, X. Liu, J. Gu, R. Si, Y. Qiu, Y. Qiu, D. Shi, F. Chen, X. Sun, J. Lin, J. Sun, Atomically dispersed Mo supported on metallic Co₃S₄ nanoflakes as an advanced noble-metal-free bifunctional water splitting catalyst working in universal pH conditions, *Adv. Energy Mater.* 10 (2020), 1903137, <https://doi.org/10.1002/aenm.201903137>.
- [59] H. Liang, A.N. Gandi, D.H. Anjum, X. Wang, U. Schwingenschlögl, H.N. Alshareef, Plasma-assisted synthesis of NiCoP for efficient overall water splitting, *Nano Lett.* 16 (2016) 7718–7725, <https://doi.org/10.1021/acs.nanolett.6b03803>.